J MATER SCI 41 (2006) 841–872

Strength and sharp contact fracture of silicon

R. F. COOK
Consultant, Minneapolis 55413, Now at: Ceramics Division, NIST, Gaithersburg, MD 20899, USA
E-mail: robert.cook@nist.gov

The fracture strength of Si is considered in the context of yield and reliability of microelectronic and microelectromechanical (MEMS) devices. An overview of Si fracture, including the strength of Si wafers, dice and MEMS elements, highlights the importance of understanding sharp contact flaws, with their attendant residual stress fields, lateral cracks and strength-limiting half-penny cracks in advanced Si device manufacturing. Techniques using controlled indentation flaws, including measurements of hardness, crack lengths, crack propagation under applied stress, and inert and reactive strengths, are applied in an extensive new experimental study of intrinsic, *n*- and *p*-type {100} and {110} Si single crystals and polycrystalline Si, addressing many of the issues discussed in the overview. The new results are directly applicable in interpreting the strengths of ground or diced Si wafer surfaces and provide a foundation for studying the strengths of MEMS elements, for which the strength-controlling flaws are less well-defined. Although the indentation fracture behavior of Si is shown to be quite anisotropic, the extensive lateral cracking greatly affects crack lengths and strengths, obscuring the underlying single crystal fracture anisotropy. No effects of doping on fracture are observed. Strength decreases in water and air suggest that Si is susceptible to reactive attack by moisture, although the effect is mild and extremely rapid. Strength increases of indented components after buffered HF etching are shown to be due to reactive attack of the contact impression, leading to residual stress relief. © *2006 Springer Science + Business Media, Inc.*

1. Introduction

The fracture properties of silicon are crucial in determining the manufacturing yield, device performance and operational reliability of microelectronic very large scale integrated (VLSI) circuits and microelectromechanical systems (MEMS). Large-scale cracking or fracture of the Si substrate at the wafer or die ("chip") level during manufacturing leads to a loss of dice ("chips") and decrease in yield when the mechanical or electrical performance of the die is compromised (even if the crack does not extend to cause complete rupture of the wafer or die). Similarly, small-scale fracture at the die or device level, remnant from the VLSI manufacturing process, leads to degraded device performance (via altered leakage current and capacitance characteristics) or reliability exposures (via eventual electrical shorts or opens). The stress driving such fracture processes can be localized (in which case it is usually associated with crack initiation), for example at sharp contacts during handling or fixturing, chemical-mechanical polishing, back-face grinding and dicing of the Si, or at small features experiencing mismatches in thermal expansion, elastic modulus or phase change with the Si. Alternatively, the stress can be global (and is then usually associated with crack propagation), for example deriving from robot handling, electrostatic chucking during film deposition, down force during chemical mechanical polishing, flexure during tape removal at back-face grind or dicing, or from thermal expansion mismatch on packaging. By their very nature, the actuator and cantilever structures in MEMS devices place Si under large stresses during operation.

At room temperature, Si is brittle and as a consequence its response to applied stress is to fracture. Breakage or failure occurs when the applied stress exceeds a critical level (the strength) for the scale of the crack or defect in the Si. Most strength-degrading cracks in Si devices are surface localized and caused by sharp particle contact from handling pins, debris generated during dicing or localized packaging contacts. Hence to optimize the performance and maintain the appropriate electrical or electromechanical reliability of Si devices, an understanding of the contact fracture process is required: What is the nature of the plastic deformation and fracture at sharp particle contacts? What happens on subsequent stressing of such contacts? These considerations are also important in cases in which controlled fracture is required (e.g., during

0022-2461 © *2006 Springer Science + Business Media, Inc.*
DOI: 10.1007/s10853-006-6567-y

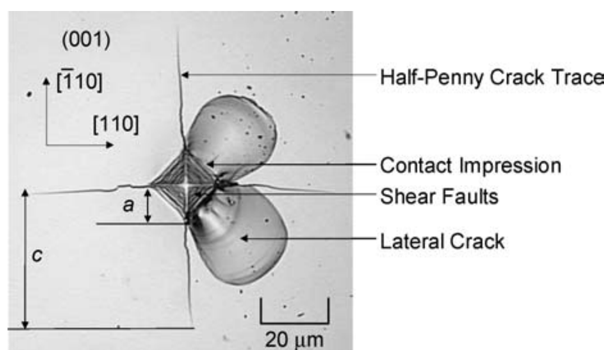

Figure 1 Optical micrograph of a (001)[110] 2 N Vickers indentation in *n*-type Si, indicating the major contact features: plastic deformation accommodated predominantly by shear faulting in the contact zone, characteristic dimension, *a*; fracture in the form of half-penny cracks, surface trace dimension, *c*; and material removal in the form of lateral-crack scallops. Such flaws control the strength of microelectronic devices through half-penny crack propagation into and across the surface in <001> and <110> directions, respectively.

the creation of cleaved surfaces for mirrors and chemical studies, precision dicing and in MEMS applications).

This paper will consider the fracture and deformation of Si at sharp contacts in some detail using controlled Vickers indentation flaws as models, Fig. 1, focusing on 10–100 μm scale defects that control the yield and reliability of microelectronic wafers and dice. The complete evolution of fracture at the contact will be considered: elastic and plastic deformation during, and residual to, indentation, leading to metastable post-indentation crack formation; superposition of an applied stress on a relaxed residual field, leading to stable crack propagation; crack instability at failure, including the effects of reactive environment, leading to contact strength degradation; and post-failure crack-path instability, leading to fragmentation. The primary vehicle for study will be $\{100\}$ oriented single-crystals, in which $\{110\}$ fracture is dominant in the $\langle 100\rangle$ and $\langle 110\rangle$ directions, Fig. 1. In this orientation, both heavily-doped *n*-type and *p*-type crystals will be examined and compared with intrinsic crystals. This orientation is predominant in the semiconductor industry for VLSI circuit and MEMS device production. The secondary vehicle for study will be $\{110\}$ oriented single crystals. This orientation is predominant in fundamental experimental and theoretical studies as fracture on the primary $\{111\}$ cleavage plane in the $\langle 110\rangle$ and $\langle 112\rangle$ directions is dominant. The tertiary vehicle for study will be polycrystalline material. Such material is predominant in the production of solar energy devices.

This paper is divided into two related parts: The first (section 2) is an overview of Si fracture in the context of microelectronic devices, extending just over the 40 year history of the *Journal of Materials Science*. The second (sections 3 and 4) addresses outstanding issues of Si strength highlighted by the overview in presenting new fracture results, based on techniques first published in the *Journal*, of indentation deformation and fracture, crack propagation, inert strength, reactive strength and fragmentation. Finally (section 5), some of the challenges still faced in the understanding of Si fracture strength for advancing VLSI and MEMS devices are considered.

2. Structure, deformation and fracture of Si

2.1. Background structure and properties

The crystal structure of Si is diamond cubic, consisting of a face-centered cubic lattice with a two-atom basis of (0, 0, 0) and $(\frac{1}{4}, \frac{1}{4}, \frac{1}{4})$, [1]. The atoms are four-fold co-ordinated into regular tetrahedrons, reflecting the hybridized sp^3 bonding. The $\{111\}$ planes are close packed and the ratio of the number of bonds per unit area crossing the $\{111\}$, $\{110\}$, $\{112\}$ and $\{100\}$ planes, respectively, is 1:$\sqrt{3/2}$: $\sqrt{2}$: $\sqrt{3}$ [2]. Fig. 2 is a schematic diagram of the structure, set into a $[110]-[\bar{1}10]-[001]$ coordinate system to be used throughout that is more convenient for Si fracture studies (cf Fig. 1) than the conventional $\langle 100\rangle$ unit cell coordinates.

The elastic properties of Si single crystals reflect the underlying anisotropy of bonding, giving rise to a direction-dependent Young's modulus *E*. In particular, the modulus anisotropy is easily assessed through examination of the variation in a $(1\bar{1}0)$ plane, which contains the four primary low-index directions: [001], [112], [111] and [110],

$$E = E_{[110]}/\left[1 + (S/E_{[110]})m^2(3m^2/2 - 1)\right] \quad (1)$$

where $S = (s_{11} - s_{12} - s_{44}/2)$, m is the direction cosine relative to [001], s_{11}, s_{12} and s_{44} are the three independent elastic compliance values referred to $\langle 100\rangle$ directions and $E_{[110]} = (s_{11} - S/2)^{-1}$ is the Young's modulus in the [110] direction [3]. Fig. 3a shows the variation in

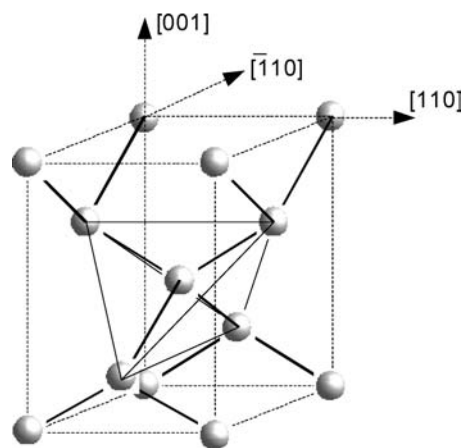

Figure 2 Schematic diagram of the crystal structure of silicon; atom positions are shown as spheres, bonds as bold solid lines and the tetrahedral coordination outlined by the fine solid lines. A tetragonal sub-cell useful in consideration of fracture of wafers and dies in microelectronics, is bounded by $(a/\sqrt{2})[\bar{1}10]$, $(a/\sqrt{2})[\bar{1}\,10]$ and $a[001]$ vectors of the conventional diamond-cubic unit cell, indicated by the dotted outline.

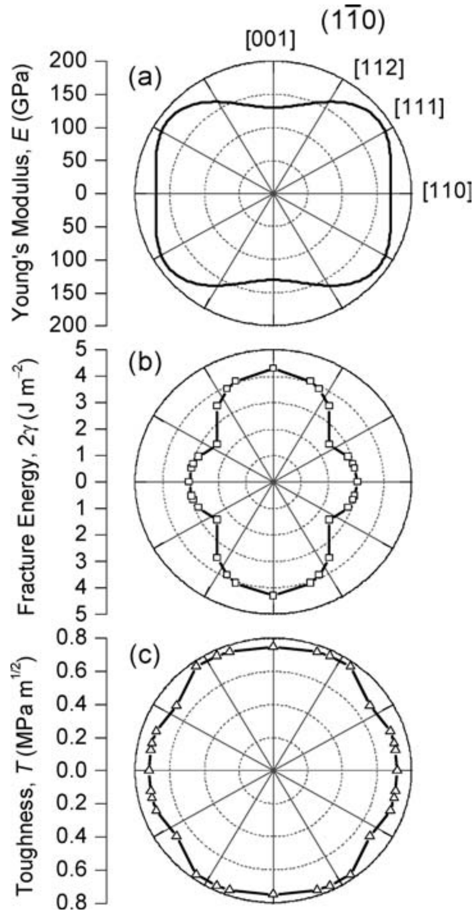

Figure 3 Plots showing the orientation dependence of (a) Young's modulus, E, (b) fracture energy, 2γ, and (c) toughness, T, of Si, projected into the (1$\bar{1}$0) plane, from Equations 1–3 . The coordinate system is the same as that in Figs 2 and 4 such that a (110) fracture plane, predominant in semiconductor processing, is normal to the page, propagating from top to bottom.

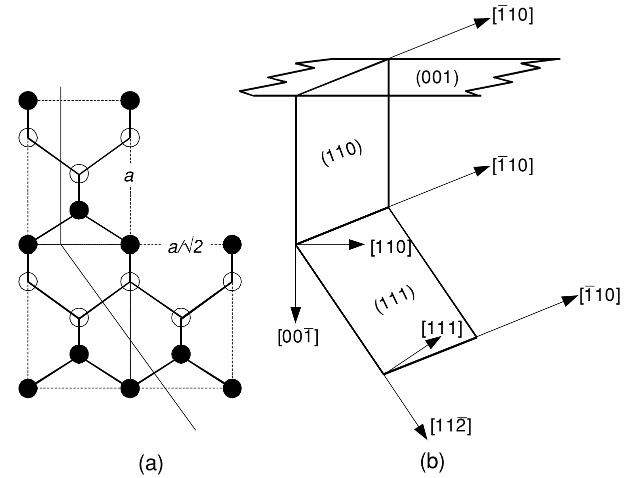

Figure 4 Schematic diagrams illustrating crystallographic cleavage planes in Si relative to an (001) wafer surface commonly used in semiconductor processing. (a) Elevations of the sub-cell from Fig. 2 in the same coordinate system; solids symbols represent atom positions in the front and rear planes of the sub-cell, open symbols at the mid-plane. (110) cleavage is through bonds inclined to the fracture surface and (111) cleavage through bonds normal to the fracture surface; the ratio of the bonds broken per unit area is $\sqrt{3/2}$, respectively, consistent with Equation 2. (b) Secondary (110) and primary (111) cleavage planes, along with the wafer surface, lie in the $\lfloor\bar{1}10\rfloor$ zone, allowing for easy rectilinear die formation along <110> directions and the possibility of tilt during crack propagation from secondary to primary cleavage.

Young's modulus for Si in the (1$\bar{1}$0) plane using Equation 1 and s_{11} = 7.68 TPa^{-1}, s_{12} = –2.14 TPa^{-1} and s_{44} = 12.56 TPa^{-1} [1]; the two-fold symmetry in this plane is obvious. The moduli vary from 187 GPa in the ⟨111⟩ directions to 130 GPa in the ⟨100⟩ directions, with an intermediate value in the ⟨110⟩ directions of 169 MPa. The average polycrystalline modulus, calculated as the mean of Hashin-Shtrickman bounds [4], is 163 GPa.

The fracture properties of brittle materials such as Si also reflect the underlying anisotropy: A simple, purely geometrical, bond-counting estimate suggests a method for estimating the fracture surface energy or fracture resistance, 2γ, for cleavage on crystalline planes [5], Fig. 4a. The variation in the fracture resistance, $2\gamma_{(hkl)}$, calculated from the number of broken bonds required to form a cleavage plane on (hkl) in the [$\bar{1}$ 10] zone, is given by [2]

$$2\gamma_{(hkl)} = 2\gamma_{(110)}[2\max(h,l)/(2h^2 + l^2)]^{1/2}, \qquad (2)$$

where planes in the [$\bar{1}$ 10] zone are of the form (hhl), Fig. 4b, and $2\gamma_{(110)}$ is the fracture resistance of the (110) plane. This predicted variation is shown as the open symbols in Fig. 3b, using $2\gamma_{(111)} = 2.48$ J m^{-2} [6, 7], recognising that the angular variation is for planes perpendicular to the directions indicated at discrete values of $m = l/(2h^2 + l^2)^{1/2}$ (the line is a guide to the eye). The fracture resistance increases weakly to 3.0 J m^{-2} for the (110) plane and somewhat more strongly to 4.3 J m^{-2} for the (001) plane.

The toughness of a particular plane may be approximated by [8]

$$T_{(hkl)} = \left(2\gamma_{(hkl)}E_{[hkl]}\right)^{1/2}, \qquad (3)$$

where $T_{(hkl)}$ is the (plane-stress) toughness of the (hkl) plane and $E_{[hkl]}$ is the Young's modulus in the (perpendicular) [hkl] direction, noting that relationships between energy- and stress-based measures of driving and resisting influences in fracture are not straightforward in elastically anisotropic materials [9]. Values for various planes are shown in Fig. 3c using the data from Fig. 3a and b. The countervailing maxima and minima in the modulus and fracture resistance variations lead to a very small variation in toughness with fracture plane; from $T_{(001)}$ = 0.75 MPa m$^{1/2}$ to $T_{(111)}$ = 0.68 MPa m$^{1/2}$. The fracture resistance and toughness values for polycrystalline materials (assuming random transgranular fracture and averaging over the planes in Fig. 3) are 3.3 J m^{-2} and 0.73 MPa m$^{1/2}$, respectively.

The plastic deformation properties of Si of interest here are those associated with sharp indentation and its large imposed shear strains and hydrostatic constraint [10]. Although dislocation mobilities are highly anisotropic in Si, and depend critically on doping level, there is very little evidence to suggest that these effects, although easily observable at sharp indentations [11, 12], are reflected in the overall sharp contact response. During sharp-contact loading, deformation is both elastic and plastic [13], with elastic deformation distributed in the material bulk, both within and without a contact area of characteristic radius a (Fig. 1). At room temperature, plastic deformation is localised in a zone beneath the contact area, of volume approximately $10a^3$ [12, 14–18], with the majority of the plastic strain carried by inhomogeneous constrained shear faulting (mode-II cracking) on approximately $\{013\}$ planes for a (001) indentation. The [100] and [010] surface traces of these faults are visible in Fig. 1 and elsewhere [15, 17], but cross-sectional observations (such as those performed with large indentation loads for halides and glasses [19, 20]) are difficult for three reasons, all of which bear on the strength of Si as controlled by sharp-contact flaws. First, cracking at the contact, particularly lateral cracking with its attendant removal of material (Fig. 1), including the plastic deformation zone periphery, renders sectioning difficult. Second, material in, and adjacent to, the plastic deformation zone has a large, tangled, dislocation density [14–18], which carries a minority of the plastic strain but renders transmission electron microscopy difficult. (These dislocations are separate from the well-defined dislocation rosette patterns [11, 12] generated at high temperatures.) The third reason concerns the magnitude of the mean resolved contact stress, or hardness, H ($= P/2a^2$ for a Vickers indenter, where P is the contact load). For Si, $H \simeq 10$–13 GPa (see next section) such that pressures generated during contact exceed those for phase transformation from the semiconducting, diamond-cubic structure to metallic, β-Sn (8–9 GPa) and other high-pressure phases [14, 16, 18]. This has the consequence that contact deformation is influenced by metal-like flow in these phases, often leading to extrusion of material from sharp indentation [16, 18] and scratch [21–23] edges, further complicating the residual contact pattern.

Deformation during sharp-contact unloading of Si is primarily elastic [13], with recovery occurring both axially in the indentation depth, h [12] and (for pyramidal indentations) transversely along the less-constrained contact impression edges. Such recovery is visible as the "pin-cushioning" of the residual impression in Fig. 1 and elsewhere [12, 14–17]. (Minor amounts of deformation during unloading are associated with reverse phase changes [13], although frustration of these often leads to amorphization of material beneath the contact [14, 16, 18].) The load-displacement, P-h, behavior of Si on sharp indentation [13] is thus intermediate between the completely elastic response associated with blunt ("Hertzian") contacts [10], and the completely dissipative response associated with sharp contacts on soft metals [24]. Such intermediate recovery leads to the existence of a residual stress field in the material that is responsible for the initiation and propagation of cracks during contact and their stabilisation after contact [25, 26]. However, as might be anticipated from Fig. 3, although the fracture patterns at sharp (and blunt [27]) indentations change significantly with the indented surface and indenter orientation, neither the hysteretic P-h behavior measured during contact nor the H values determined after contact are observed to depend significantly on doping, the indented surface or orientation of the indenter [13] or scratch [21]. This lack of contact deformation anisotropy in Si is a consequence of the facts that beneath indentations: elastic strain fields are multi-axial (such that the polycrystalline modulus is often a good approximation for single crystal indentation moduli [28]); plastic deformation by dislocation motion is suppressed at low temperatures; and, fracture of shear faults by propagation along low energy cleavage planes is rare.

Table I compares the mechanical properties of Si with those of some other microelectronic materials. The picture that emerges is that of a material that is more "ceramic"-like in its mechanical properties than "metal"-like. Although stiffer and harder than other materials used in microelectronics, as indicated by the greater E and H values, the fracture resistance, R, of Si is simply the surface energy, 2γ, similar to that of SiO_2 glass, rather than dominated by dissipative plastic deformation processes as in Cu and Al. In fact, the increased modulus of Si relative to SiO_2 offsets its decreased fracture resistance to leave both materials with similar toughness values $T = (RE)^{1/2}$, approximately 0.7 MPa $m^{1/2}$. The modulus/hardness ratio, $(E/H)^{1/2}$, provides an (inverse) measure of the coefficient of restitution and degree of depth recovery at a contact and

TABLE I Mechanical properties of microelectronic materials

Material	Young's modulus, E (GPa)	Hardness, H (GPa)	Fracture resistance, R (J m^2)	Recovery ratio, $(E/H)^{1/2}$	Brittleness index (RE/H^2)	Coefficient of thermal expansion, α (ppm $^{\circ}C^{-1}$)
Si (crystalline)	130–187	10	2.5–4.3	4.1	5 nm	3
SiO_2 (amorphous)	72	6	8.8	2.9	18 nm	0.6
Cu (polycrystalline)	128	0.4	10^3	18	0.8 mm	18
Al (polycrystalline)	72	1	10^4	8.5	0.7 mm	23

again suggests that residual contact impressions and stress fields in Si are less like metals and more like SiO_2, with large degrees of recovery. The similarity to SiO_2 during contact is particularly strong when the brittleness indices, RE/H^2 are compared. The brittleness index provides a measure of the length scale at which a material ceases to accommodate contact deformation by elastic and plastic processes alone and begins to fracture (i.e., it is the largest contact before cracking). The very small length scale for Si, similar to that of SiO_2 and a factor of 10^5 smaller than those for Cu and Al, point to the brittle nature of Si and to the almost certainty of fracture at most contacts. The stiff, covalent bonds underlying the Si mechanical properties are also exhibited in the thermal properties, with the thermal expansion coefficient of Si substantially less than those of Cu or Al.

2.2. Fracture of Si ingots

There are many previous studies of contact-mediated fracture and strength of Si, a considerable number related to yield and reliability of VLSI circuit and MEMS elements during manufacturing and operation. It is useful to review these, and the current work, to place both in the broader context of studies of Si fracture. A key feature in these discussions is a *characteristic* limiting defect size, c_f, associated with the failure stress or strength, σ_f, of a component. The scaling between c_f and σ_f is [29]

$$c_f = \left(\frac{T}{\psi \sigma_f}\right)^2, \tag{4}$$

where ψ is a dimensionless geometrical constant. Representative values for Si surface flaws in tension are $T = 0.7$ MPa $m^{1/2}$ and $\psi = 1$.

The largest length scale associated with Si fracture is that of the melt-grown ingot [30, 31]; such cylindrical ingots can be over 1 m long × 0.3 m in diameter and weigh over 160 kg. Blunt, elastic contacts with the ingot can lead to cm-scale surface ring cracks and sub-surface cone cracks [27, 32], not usually visible on the ingot surface, leading to a loss of usable Si on slicing to form wafers. Gravity loading during stacking or standing of ingots, or bumping of ingots with even moderate handling velocities, are sufficient to develop the 10 kN-scale static or impact forces required for initiation of such cracks from pre-existing defects on the ingot surface [30], even if the surface defects are comparable to those limiting the ~2 GPa strengths of Si whiskers [33]. Such defects are of order $c_f \sim 0.12$ μm.

2.3. Fracture strength of Si wafers

The second length scale associated with Si fracture is that of the sliced wafer [31], which are of order 0.7–0.8 mm thick × 200–300 mm in diameter and weigh 50–125 g. Wafer manufacturing involves sawing from the ingot, grinding and lapping to size and flatness, etching to remove surface impurities and polishing to remove surface defects, typically arriving at a mirror surface finish with sub-nm-scale average roughness on which devices are to be constructed. On careful treatment and handling this surface remains with the largest, strength-limiting defects comparable to those in the whiskers: strengths of 2–4 GPa were measured for small, ~5 mm, plates from (001) and (111) wafers [34, 35]. At these strength levels, the plates fragmented into many pieces at failure (including Si dust), an observation dating back to the earliest studies on glass fibers [29]. There is no doubt that the large strengths were obtained through the use of small samples, such that the probability of encountering a large defect in the ~1 mm^2 stressed area was small—an observation also made in the earlier studies of Si rods and whiskers [33] and glass fibers [29]. Tests of whole, but small, (111) wafers with ~300 mm^2 stressed area exhibited polished-surface mean strengths of ~1 GPa with large scatter, 0.5–2 GPa [36]. Decreases in both the mean strength and the relative scatter were observed, to ~330 ± 50 MPa for (001) wafers that were lapped but not polished [34, 36], down to ~200 ± 40 MPa for wafers that were in the raw, as-sawn state [36]. Similar results were observed for small polycrystalline Si wafers tested with ~3 mm^2 stressed area: wafers with etched surfaces exhibited strengths of ~300 ± 30 MPa that decreased to ~80 ± 3 MPa for wafers that were in the raw, as-sawn state [37]. The effective defect size in the as-sawn small single-crystal wafers was of order $c_f \sim 12$ μm and that for the polycrystalline wafers, $c_f \sim 75$ μm. Tests on full size wafers, with ~15,000 mm^2 stressed area, exhibited even greater strength decreases: polished wafers exhibited a strength of ~120 ± 5 MPa, etched wafers ~90 ± 30 MPa, and as-sawn wafers only ~12 ± 2 MPa [38]. The effective defect size in these as-sawn full-size wafers was of order $c_f \sim 3.5$ mm.

The picture that emerges is that it is possible to prepare almost-pristine Si wafer surfaces over small areas by polishing and careful handling. Such surfaces have strength-limiting defects of order 0.1 μm, about 100 times the surface roughness, leading to strengths in the GPa range. However, under normal handling circumstances, over large areas comparable to that of the wafer, there is likely to be a defect of order 50 μm, about 1/10 of the wafer thickness, leading to strengths of order 100 MPa. Treating the strength of polished Si surface as an intrinsic parameter [31] allows a relationship for wafer survival to be established between the component- (wafer-)level extensive parameters of fixturing geometry, applied load and wafer thickness: A design strength of 130 MPa for a (001) wafer seems appropriate in this regard. With geometry specified, load and thickness can thus be determined for optimising manufacturing performance in terms of ingot yield of (unbroken) large wafers [31]. With wafer thickness specified, fixturing geometry and temperature gradients can

be determined to maximise wafer yield in the presence of gravitationally- and thermally-induced loads [39].

Deliberate surface treatments such as grinding introduce large mm-scale defects, comparable to the wafer thickness, and strengths of order 10 MPa. Cross-sectional observations of the damage zone introduced by, or remnant from, surface treatments support this view. In the full-size wafer study above [38], the maximum depth of damage remnant from sawing was ~27 μm, this was decreased to ~ 3 μm on etching and <0.5 μm on polishing. In an earlier study on (111) small wafers, tested with ~20 mm^2 stressed area, strengths were similarly observed to decrease from ~135 to ~75 MPa as the depth of damage increased from ~10 to ~20 μm with change in the crystalline orientation [40]. These measurements reinforce the ideas that observable "damage" in a Si component will probably be smaller than the strength-controlling crack size, consistent with indentation observations [26], and that sharp-contact mediated fracture strength in Si depends on crystallographic orientation.

2.4. Fracture strength of Si dice

The third length scale associated with Si fracture—and probably the most important—is that of the diced chips or dice; small quadrilateral plates, 0.2–0.8 mm thick × 1–200 mm^2 in area. Die manufacturing involves the formation of the VLSI circuits or MEMS structures on the front or active side of the wafer by successive deposition and removal of lithographically patterned metal, dielectric and polymer layers, back-side grinding (BSG), lapping and etching of the wafer to obtain the required die thickness and back-side surface finish, high-speed sawing (dicing) of the wafer to separate the dice, and sorting and picking of dice according to electrical, optical or mechanical performance of the active devices (the final two operations are often combined into dice-sort-pick: DSP). BSG and DSP are often the most critical steps in determining overall Si yield (acceptable finished dice per wafers started in the manufacturing process): they involve mechanical loading of entire, front-finished (therefore maximum value) wafers in fixturing and deliberate high-velocity sharp-particle contact, including that from debris, in grinding and dicing.

The strength-limiting defects introduced by BSG (particularly in the early, gross material removal stages) [41–44], the warpage often induced by imbalanced grinding and active layer stresses and uneven thinning [42, 45] and the thinning itself all lead to inter-related smaller strengths and greater imposed stresses through the BSG and DSP processes. Back-side fracture tests after BSG treatments on full thickness dice [41] and thinned dice [42, 43] or wafers [44], with ~1–2 mm^2 stressed area, agree qualitatively with the wafer observations: coarse grinding significantly reduces strength, subsequent fine grinding increases strength and etching increases it even further (leading to die fragmentation on failure [41]). More direct comparison of die-scale results with wafer strengths is difficult, however, as die results are often reported in terms of failure loads observed in test geometries that are operationally relevant and thus easy to implement [41, 42], but which are difficult to analyse. A further complication in comparing die-scale failure behavior with that of wafers is that the dicing process introduces an additional defect population that is often sampled in the test geometries used for die strength measurement. To this stage, the quoted strength measurements have all been obtained through (equi-)biaxial loading of the central area of a plate, remote from any edges (usually by loading a spherical punch or circular ring onto the center of the circularly-supported wafer or die). However, a rectangular die is conveniently, and relevantly, tested through uniaxial loading of the central area as a bar, including the edges (usually in three- or four-point bending). Hence, additional strength-controlling edge defects introduced by dicing will be sensed in uniaxial testing and not in biaxial testing (whether such defects are literally introduced by sharp dicing contacts on the die edge or are simply surface flaws rendered more potent by the lack of constraint at the die edge).

Tests on (001) dice in [110] uniaxial loading [46] showed the effects of superposing a dicing-induced edge-flaw population with a broad strength distribution, ~310 ± 110 MPa, onto a surface-flaw population remnant from grinding with a narrow distribution, ~ 290 ± 40 MPa. The total strength distribution of the finished dice reflected a change in the dominant flaw at different strengths arising from the difference in distribution of the separate flaw populations about similar means. There was a low probability of small (<200 MPa) die strengths (controlled by large, but rare, dicing defects) and a high probability of moderate (~300 MPa) die strengths (controlled by small, but common, grinding defects). The high (> 400 MPa) die strengths associated with the ultra-small, rare dicing defects were not observed in the overall distribution; they were eclipsed by the common, smaller strength, grinding flaws. (The existence of the high strength dice was inferred from biaxial strength tests with the same stressed area that allowed the dicing and grinding distributions to be separated.)

The relative probabilities of edge and surface flaw failure and observed strength levels can also depend on die position on the wafer, as position dictates the orientation of grinding striations relative to the die axes. Uniaxial die strengths are smaller when grinding striations are perpendicular to the loading direction, usually the long axis [43, 47]. Hence a die with striations perpendicular to the long axis will exhibit a small, surface-controlled strength whereas a die with striations parallel to the long axis will exhibit a large, edge-controlled strength: the effective sur-

face defect size can be characterised by a striation orientation dependence for Ψ in Equation 4. Direct assessment of edge-flaw strength distributions can be performed by twist loading a plate (in four-point anticlastic bending) to place the edges in tension and the central surfaces in shear. Twist tests showed an edge strength distribution of ~60 ± 8 MPa for single-crystal and ~45 ± 15 MPa for polycrystalline laser-diced Si plates [48], suggesting that laser dicing introduces much more potent edge defects than conventional saw dicing.

The picture that emerges here is that wafers exiting the active-face segment of manufacturing are reasonably strong (~200 MPa) but are then weakened significantly (to ~50 MPa) by the introduction of large surface flaws in the early stages of BSG, before restoration to full strength in the later stages of BSG (although *loads* the now thinner wafers are able to withstand are much smaller). Subsequent dicing leads to the introduction of new edge defects that can weaken a die in uniaxial loading (to ~100 MPa). A substantial motivation in the wafer-finishing studies above was thus not just successful movement of the substrate wafers through active-device processes in the manufacturing line, but successful movement of wafers and dice through BSG and DSP.

The die-scale consideration, however, that provides the most significant motivation for study of sharp-contact mediated fracture of Si, is the stress that is generated in a die on packaging [49, 50]. A package for a die provides appropriate mechanical support, environmental protection and electrical, optical and thermal interconnection between the active elements on the die and the external system (e.g., telephone, computer, automobile or toaster). Heating and cooling during the packaging process [49] or subsequent thermal cycling [50] usually generates considerable stress in the die from thermal expansion mismatch between the die and an element of the package (typically the polymeric, ceramic or composite substrate in concert with a polymeric or composite encapsulation or adhesive layer). If the stress generated is greater than the die strength remnant from BSG and DSP, failure will occur. A study of uniaxial die strengths, combined with an analysis of packaging stress, showed that while BSG surfaces were weaker, ~210 MPa, than bare or etched, ~350 MPa, the greatest probability of failure on packaging derived from rare, large defects generated in DSP on picking [49]. These defects reduced the strength significantly, to ~90 MPa, uncomfortably close to the stress calculated on packaging, ~75 MPa. An analysis of stress induced on thermal cycling of a package [50] showed that while calculated die stress at room temperature was ~50 MPa, that at -40°C was ~90 MPa: the conclusion that in order to survive thermal cycling the die should be *both* thin and have few back-side flaws serves to emphasise the importance of understanding sharp-contact fracture of Si.

2.5. Fracture strength of Si MEMS elements

The fourth length scale associated with Si fracture, and the most recently studied, is that of the elements in MEMS devices: small beams, plates, columns and gears, 1–1000 μm in scale. MEMS devices are formed by similar lithographic deposition and removal sequences to those in VLSI circuit manufacturing, but the materials are predominantly polycrystalline and single-crystal Si and the MEMS elements are formed by vapor (typically isotropic) or liquid (typically anisotropic) etching. Concerns with the fracture properties of Si are directly related to performance here, as the function of MEMS elements is structural; they are designed to generate and support loads and displacements in application. (As opposed to the indirect, but still crucial, concerns for VLSI circuits; Si is just the platform for the microelectronic or photonic functional elements and loads and displacements encountered by the Si during manufacturing or application just have to be survived.) The etched surfaces of the elements have surface roughness of ~1–100 nm, leading to very large measured strengths of specially formed single-crystal beams, ~1–18 GPa [51–55], shafts, ~20 GPa [56], plates, ~4 GPa [57], membranes, ~1–7 GPa [58] and rods, ~0.5–1 GPa [59, 60]; comparable to the strengths measured in bending of the free rods and whiskers some 30–40 years earlier [33].

In the case of the beams and plates, increased strengths were correlated with decreased surface roughness [52–55, 57], but the characteristic defect size of $c_f \sim$ 1–30 nm precluded identification of the strength-controlling flaws, especially as the fracture surfaces of the large-strength samples were extremely rough. Tests on specially-formed polycrystalline rods showed similarly large strengths, ~0.6–2.8 GPa [61, 62], and small strengths were again correlated with increased surface roughness. The relatively small strengths of some membrane structures [58] and the rods [59–62] relative to the other loading geometries were caused by the powerful stress-concentrating action of re-entrant corners at the membrane periphery and rod gauge ends, leading to failure at these points. The etching processes used to form MEMS elements probably generate corner radii of near-atomic dimensions, suggesting that an important load-limiting effect is the stress-concentration field of a sharp notch, noted in an early beam study [51]. Two approaches to model this effect have been successful: By calculating the enhanced stress field at corners of deliberately varied radii (0.25–1.4 μm), the $c_f \sim$ 10 nm, strength-limiting defects in the membrane were shown to be invariant with corner geometry, all leading to ~7 GPa strengths [58] (~1 GPa strengths were observed for membrane structures containing unmodified sharp corners, suggesting a change in the nature of the defect as well as the stress-concentrating nature of the structure in this case). In contrast, the sharp notch itself can be treated as a strength-limiting defect, with a

divergent stress field at the notch tip characterised by an exponent different from that for a crack and a failure criterion, somewhat similar to that of toughness, that depends on the included notch angle [59, 60, 63]. Decreases in strength with rod width, from ∼1 GPa to ∼0.6 GPa, in T structures were predicted correctly using this criterion [60], suggesting that in some cases the MEMS structural geometry itself forms the strength-controlling flaw.

In the absence of stress-concentrating features, strength-controlling flaws are distributed over the etched surfaces, leading to an expectation of increased strength with decreased element size or stressed area (and thus flaw probability), similar to that observed for bent rods [33] and biaxially-loaded wafers [34–36, 38]. Compilation of strength measurements in a recent overview [64] showed this expectation to be fulfilled for polycrystalline Si MEMS elements; strengths decreased by a factor of about two, from ∼3–4 GPa to ∼1.5–2 GPa, as the stressed area of tensile specimens increased from 10^2 μm^2 to 10^5 μm^2 (0.1 mm^2). Similar results were observed in strength measurements of single-crystal elements [54]; strengths decreased from ∼17.5 GPa to ∼0.5 GPa as the effective stressed area of the beams increased from 10^{-2} μm^2 to 10^6 μm^2 (1 mm^2) (although here as well, beams tended to break near the fixed, stress-concentrating, ends).

It is tempting to note the strength overlap of these MEMS elements with those of wafers and dice at similar stressed areas, ∼0.5 GPa at ∼1 mm^2 and infer a universal, decreasing, strength-area relationship for Si. The *physics* of this would be incorrect, however, as the use of weakest-link ideas to scale strength with the extent of stressed material requires the strength-controlling flaws to belong to the same population. The strengths of MEMS elements are controlled by etching flaws, those of wafers and dice by grinding or dicing flaws (and we have already observed above how competition between these latter two precludes simple scaling of die strength with size under uniaxial loading). The overlap, however, does point to an underlying *engineering* truth: manufacturing processes tend to scale roughness and tolerances with the size of the component being manufactured [65]. Hence, the correct inference is that wafer, die and MEMS element manufacturing processes introduce different flaw populations and that these scale with the size of the component, leading to the overall decreasing strength-component size trend; within a component type, weakest-link scaling applies.

2.6. Fracture strength of Si with controlled-flaws

The strength studies above, while providing design guidance for Si components once a manufacturing process has been established, do not allow for explicit prediction of fracture strength as a function of flaw size or for the measurement of toughness that underlies such predictions. Placement of a strength-limiting flaw with controlled size, geometry, orientation and location into a sample prior to a strength measurement overcomes these difficulties. Sharp indentations such as in Fig. 1 provide such flaws and have been used for some time to study the fracture properties of Si. Early studies [66–68] focused on measuring the toughness of single-crystal and polycrystalline Si using Knoop indentations on beams and simple inversion of Equation 4:

$$T = \psi \sigma_f c_f^{1/2} \quad (5)$$

The dimension c_f was treated literally as the controlling "Griffith" crack length [29] and inferred from scanning electron microscope images of beam fracture surfaces and the geometry parameter, ψ, thus determined from fracture mechanics considerations. Later studies in the same spirit [69–71] used Vickers indentations on single-crystal beams, taking c_f to be the surface trace of the half-penny cracks. Toughness estimates with experimental scatter of ± 5–15% from both sets of studies varied over the range 0.8 to 1.2 MPa m$^{1/2}$ for single-crystal Si and from 0.75 to 0.87 MPa m$^{1/2}$ for polycrystalline Si, agreeing with Fig. 3c to well within a factor of two. However, beyond noting this agreement, not much more can be read into these values, particularly not the widely cited, but not always replicated [68, 70], result that appears to be in accord with intuition, $T_{(100)} > T_{(110)} > T_{(111)} > T_{\text{grain boundary}}$ [66], but which Fig. 3c suggests is extremely unlikely to be detectable experimentally. In addition, systematic experimental and analytical errors were also included in these studies: the micrographs presented [66–71] make clear the extreme difficulty of objective flaw-size determination from fractographic images and neglect of the residual indentation stress field invalidates the fracture mechanics assumed to be underlying Equation 5.

Fracture mechanics of indentation flaws under applied stress, taking the residual field [25, 72, 73] into account, was developed and applied to Si [26] at about the same time as the Knoop studies. Using Vickers indentations on {111} beams in the load range $P = 5$–200 N, half-penny cracks, 12–600 μm long, were formed, leading to strengths of 160–20 MPa. These strengths are at the small end of the range observed for wafers and dice, suggesting that sharp contacts and their associated cracks are the strength-limiting flaws in sawn, ground or diced components (unsurprising, as these processes remove material by deliberate repeated sharp contact). Relations between load, crack length and strength provide the required strength prediction capability for processing of Si components leading to strength-limiting sharp contact flaws (within the constraint of common contact geometry). Use of the appropriate crack length-strength pairs in Equation 5 leads to toughness estimates of ∼0.5 MPa m$^{1/2}$, con-

siderably smaller than those above and in Fig. 3c. This is because the residual field still acted as a crack-driving force *during* the strength tests, leading to reduction of the applied stress required to cause beam failure. Evidence for the continuing action of the residual field came from direct observation of stable precursor extension of half-penny cracks on stressing, leading to an increase in the crack length at failure. Toughness estimates using indentation fracture mechanics analyses of the strength data were not made, due to an obvious reduction in magnitude of the residual field by surface chipping associated with lateral cracking, particularly at the large indentation loads: The presented crack length-strength pairs at failure give toughness estimates of ~0.8–1 MPa $m^{1/2}$; reasonably consistent with other estimates and the predictions of Fig. 3c.

Just as with the change of focus from 10 μm scale flaws, controlling the strength of wafers and dice, to 0.1 μm scale flaws, controlling the strength of MEMS elements, recent indentation-strength studies have focused on sub-μm controlled-flaws. Tests on {100} and {111} single-crystal Si plates using Berkovich indentations over the load range 1 N – 2 mN extended the range of impression sizes down to ~0.5 μm, smaller than that required to generate indentation cracks [74, 75]. (Berkovich indenters are three-sided analogues of the four-sided Vickers indenter with the same equivalent cone included angle, and therefore the same volume-to-depth ratio that dictates the indentation crack driving force [76].) Such "sub-threshold" indentations had very different strength characteristics than conventional post-threshold flaws (as in Fig. 1): failure was caused by initiation of cracks from the contact impression (rather than propagation of pre-existing cracks) and the dependence of strength on indentation load was much greater, $\sigma_f \sim P^{-2/3}$, than the ideal indentation response observed over most of the post-threshold Si indentation-strength range, $\sigma_f \sim P^{-1/3}$ [26 , 74, 75]. Strengths of plates containing sub-threshold flaws were 0.5–5 GPa, at the small end of the range for MEMS elements, suggesting that instability of very small, ~10–100 nm, crack-like flaws at stress-concentrating features are the strength-limiting defects for many MEMS elements and that there is some similarity between etch pits and sub-threshold contact impressions. These observations also reinforce the view above that different manufacturing processes introduce different flaw populations—with fundamentally different characteristics—to control the strength of Si components at different length scales.

The analytical basis of indentation fracture mechanics was developed and verified experimentally [72, 73] just prior to the seminal indentation-strength study of Si [26]. These three papers, published in the *Journal of Materials Science* just over 25 years ago, established the experimental methods and performed one of the first applications of the controlled-flaw testing philosophy to characterise a material. The experimental techniques developed therein will be used here as well and are depicted in Fig. 5: A sharp probe is loaded onto a material surface, giving rise to a hysteretic load-displacement trace over the contact cycle that can be measured [13, 24], Fig. 5a, or, more usually, of known peak load, giving rise to an indentation impression and cracks that can also be measured [26], Fig. 5b. An indented sample is then loaded in flexure, and the degradation of strength with indentation load measured [26, 73–75], Fig. 5c, or, less commonly, crack extension measured under applied stress [26, 73], Fig. 5d.

2.7. Fracture resistance of Si

It is clear that, as in most brittle materials, the strength of Si is a composite quantity, i.e., it depends on both a material-intrinsic, intensive property characterising the material resistance to fracture and (as noted above) extrinsic variables characterising both extensive and relative dimensions of the component and the stress-concentrating flaw. The earliest measurements of fracture resistance, using the well-defined double-cantilever beam geometry, of Si {111} planes were $2\gamma = 2.48$ J m^{-2} [6] and 2.50 ± 0.02 J m^{-2} [7]. These values are shown in a review of semiconductor fracture [77] to be consistent with both calculations, based on known bond-rupture energies, and experimental scaling of fracture resistance with band-gap in elemental and compound semiconductors. Subsequent measurements, also using a "long-crack," but mixed-mode (I-III), double torsion geometry of ~5.3 ± 0.3 J m^{-2} appear too large [78] (converting the reported toughness value to fracture resistance using Equation 3 and $E_{[111]} = 187$ GPa), although the fracture resistance measured for Si {110}of 3.62 J m^{-2}, also obtained using the double torsion geometry [79], compares acceptably with 3.0 J m^{-2} predicted from the earliest measurements. Measurements using "small-crack" strength and fractographic methods similar to those described in the previous section gave 2.28 ± 0.28 J m^{-2} for the fracture resistance of Si {111} [80], which compares well with the earliest measurements, but again, other measurements for Si {110} were larger than predicted: 3.8 ± 0.4 J m^{-2} [80] and 5.3 ± 0.8 J m^{-2} (converting the reported toughness value [81] to fracture resistance using Equation 3 and $E_{[110]} = 169$ GPa). (The Knoop indentation based fractographic estimates above [66] were similarly larger: 3.6 J m^{-2} for Si {111}, 4.8 J m^{-2} for Si {110} and 3.5 J m^{-2} for polycrystalline Si.)

While it can be argued that fractographic measurements may systematically misestimate the flaw size at failure and use the wrong mechanics, overestimating fracture resistance, more recent measurements, using small specimens prepared using MEMS techniques show improbably large values for a different reason. Values reported of 6–16 J m^{-2} [82] and ~8 ± 2 J m^{-2} [83] for Si {110}, ~18 ± 8 J m^{-2} [84] for Si{100}

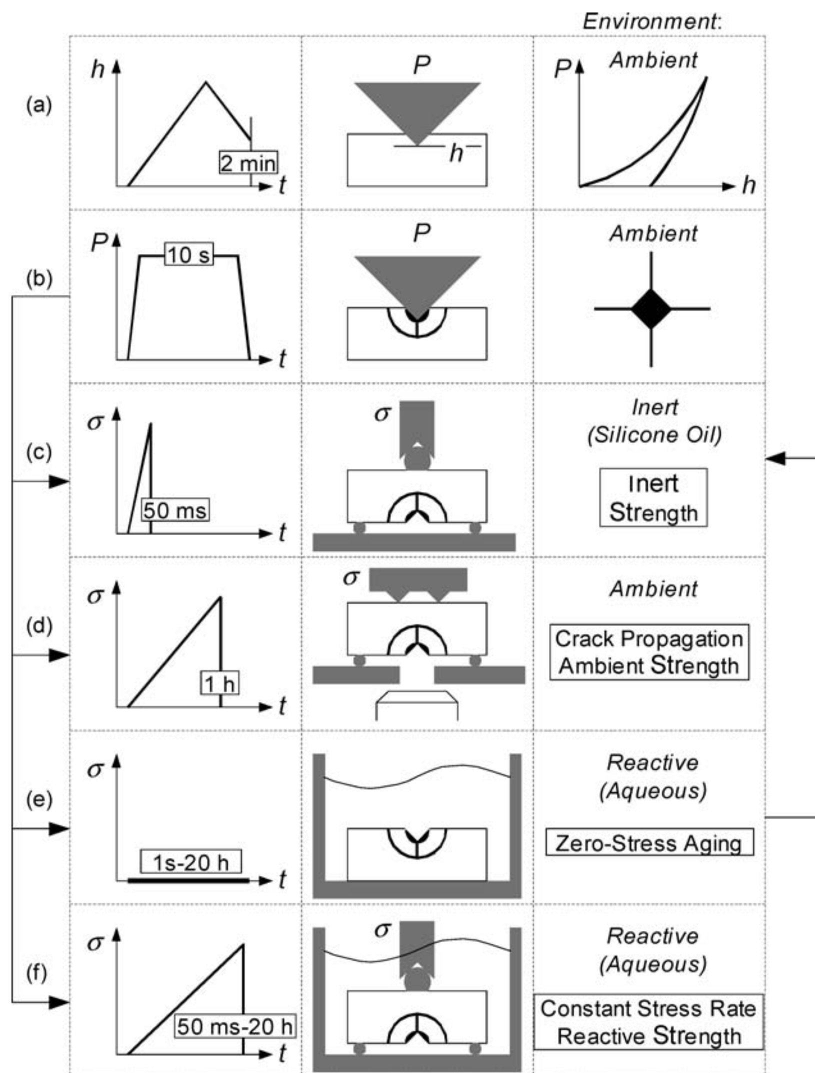

Figure 5 Schematic diagrams illustrating the mechanical variables, time scales, geometries and environments of the various testing techniques used here to study sharp-contact mediated fracture strength of Si: (a) Displacement-controlled instrumented indentation testing (IIT); (b) Gravity-loaded (conventional) indentation; (c) Strength testing of indented samples in moisture-free inert environment; (d) Crack propagation measurement in ambient air environment; (e) Aging in reactive environment with subsequent inert-strength testing; and (f) Strength testing with constant applied stressing rate in reactive environment.

(converting reported toughness values) and 16–62 J m^{-2} for polycrystalline Si [85] reflect assumed sharp crack-tip geometries that were not actually realised in the MEMS test structures. Instead, just as with the MEMS [58–62] and sub-threshold [74, 75] strength studies above, these values reflect criteria for initiation of failure from very small cracks at the roots of stress-concentrating notches (a strength test), rather than the criterion for propagation of the assumed cracks (a fracture resistance test); the large experimental scatter probably reflects the variability in local geometry of the small crack and the notch tip. In fact, tests on large polycrystalline Si compact tension specimens, with diamond-sawn notch tips of known 150 μm radii [86], exhibited apparent fracture resistance values of $\sim$17 $\pm$ 8 J m^{-2} and exhibited distributions in these values similar to those observed in strength tests [64]. Values reported for a Si $\{110\}$ MEMS fracture resistance geometry above [82] exhibited a similar distribution. However, measurements on MEMS polysilicon rods, in which measured μm-scale cracks were deliberately introduced by an offset indentation technique prior to stressing, gave fracture resistance values of 4 $\pm$ 0.5 J m^{-2} (converting the reported toughness) [87], consistent with the macroscopic measurements above. Tests on un-cracked rods of the same material containing notches with 1.1 μm radii exhibited strengths of 4.0 $\pm$ 0.6 GPa, with clear fractographic evidence that the flaws at the notch root responsible for failure were $<$0.3 μm in scale, further confirming that many MEMS fracture resistance measurements are better interpreted as strength tests.

At high temperatures, above ∼700°C, Si can exhibit extremely large fracture resistance values, ∼80 J m^{-2}, as the material undergoes a brittle-ductile transition (BDT). The fracture resistance observed depends on both temperature and loading rate and is associated with the initiation and limited propagation of dislocations from the crack tip, leading to shielding of the crack and perhaps blunting of the tip. The fracture resistance of the sample in these cases is thus an apparent value, reflecting the kinetics of the dislocation emission, glide and shielding processes in the bulk of the material superposed on the intrinsic resistance associated with bond rupture to form the crack surface. Models of the toughening observed above the BDT temperature assume that the cracks are sharp and have fracture resistance values characterised by the intrinsic bond-rupture values discussed above. Observations of crack tips in Si formed at room temperature exhibit no dislocations and appear atomically sharp; dislocation effects do not affect fracture resistance at room temperature (for a review of crack-tip dislocations and the BDT in Si see [77]).

Overall then, it appears that the fracture resistance measurements of Si first reported [6, 7] are the least ambiguous from a testing geometry perspective (pure mode-I, primary cleavage plane, known crack geometry) and in best agreement with independent semiconductor bonding information. Over the intervening 40+ years, alternative test methods have tended to yield values larger than those first measured or predicted. Ironically, the most recent tests on samples prepared using advanced manufacturing methods, while providing critical information on the likely failure loads of MEMS components, are least able to provide fracture resistance measurements of the constituent materials.

2.8. Fracture of Si under reactive conditions

As might be anticipated for a material with predominantly covalent, apolar bonds, Si is immune to non-equilibrium slow crack growth (stress-corrosion cracking) in water and other solvents. Such non-equilibrium cracking can occur when specimens are loaded in reactive environments at crack driving forces less than the fracture resistance, leading to delayed failure under sub-critical loads. Direct observations in Si show no such crack extension: The earliest double cantilever beam fracture resistance measurements [7] exhibited no crack growth prior to catastrophic failure at instability (when the crack driving force exceeded the fracture resistance) when held under static load in air or N_2 gas for more than several hours. Tests on specimens containing indentation cracks held in air and water under loads up to 99% of the critical level (as in Fig. 5d) exhibited no crack extension [26, 88]. The pre-cracked MEMS polycrystalline rods above [87], held under static loads approaching the critical level in 90% relative humidity air for 30 days exhibited no crack extension. Indirect tests also imply no such extension: Beam specimens containing indentation flaws held in water, acetone or aqueous solutions of NaCl, HN_4OH and HNO_3 under load at 95% of the critical level for two weeks exhibited no delayed failure [89]. Displacement-controlled double-torsion specimens containing long cracks exhibited no load relaxation or acoustic emission associated with crack extension prior to the critical displacement level [78]. Biaxially stressed plates containing indentation flaws (as in Fig. 5f) exhibited no dependence of the failure stress on stressing rate or difference between air and water environments [90, 91].

Direct measurement of crack extension in a Si MEMS double-cantilever beam specimen has been made in air [94], but the erratic stop-start nature of the propagation and the large range of crack velocities observed over the small range of crack driving force levels at or close to the fracture resistance suggests that these measurements were of post-critical, not sub-critical, growth. Prior claims of slow crack growth in Si come from indirect measurements, in which compliance changes were used to infer crack extension: it is probable that either another part of the test rig was relaxing in the early double-torsion load-relaxation experiments [93] or some material other than Si was cracking prior to failure in the later MEMS cantilever beam fatigue experiments [94]. An overview and fracture mechanics analysis of such fatigue experiments [95] shows in fact that the competing effects of silicon oxide growth and stress-corrosion cracking of the oxide explain the time-dependent fracture effects observed at the small length scales of MEMS elements.

Stress-corrosion cracking and delayed failure of silica and other oxides in water and air, observed in the earliest studies on glass fracture [29], are well explained by a reaction between polar H_2O molecules and the polar Si–O–Si bonds, which become more polarised by the large strains at a crack tip [96]. The reaction forms easily broken hydrogen-bond Si–OH···HO–Si pairs at the crack tip, leaving the newly-formed fracture surface terminated by Si–OH silanol groups in a lower energy state (relative to unterminated Si– and Si–O– states obtained in inert environments). Molecular orbital simulations [97] using clusters of atoms suggest that Si–Si crack-tip bonds do not become more polarised under strain and have little reaction affinity with water molecules (and therefore Si should not exhibit stress-corrosion cracking in water). Hybrid quantum mechanical-molecular dynamics simulations [98] using larger numbers of atoms in Si crystal structures, do suggest, however, that there can be strain-dependent charge transfer effects between H_2O and Si, leading to the formation of Si–O–Si crack tip structures and Si–OH surface terminations (and therefore Si could exhibit stress-corrosion cracking in water).

Regardless of the disagreement between the simulations, the requirement of a polarised Si–Si crack-tip bond for reaction and stress-corrosion cracking of Si in polar solvents is common. Such polarised bonds do occur in

Si during oxide removal, surface cleaning and stabilisation of wafers by aqueous HF etching [99–101]. Once the surface oxide has been removed [101], but before the surface is terminated with stable, low-energy Si–H pairs [99], an intermediate step in such Si etching is the formation of polarised “back bonds” [100] between surface Si–F pairs and Si atoms in the underlying layer: $Si^{(\delta-)}$–$Si^{(\delta+)}F$. Such bonds are susceptible to HF reaction and thus stress-corrosion cracking of Si in HF solutions seems possible: HF can dissolve the surface oxide, temporarily terminating the Si surface with the polarised back bond structure, before continued HF attack removes the surface Si and terminates the underlying Si with H. This mechanism does not require any strain-enhanced polarisation or reactivity and actually removes material; the emphasis is less on “stress” than “corrosion” cracking. Nevertheless, growth of lateral cracks has been observed in indented Si samples exposed to HF solutions [102], consistent with this idea.

2.9. Fracture of Si under dynamic conditions

As a crystalline material exhibiting no dislocation motion at room temperature and little reaction with normal environmental species, Si has long been regarded as the ideal brittle material from both experimental [6] and computational [103] viewpoints. The development of high-speed data acquisition and computational systems, along with well-tested interatomic potentials, has extended study beyond the static equilibrium of these earlier works to dynamic crack propagation at crack driving forces greater than the equilibrium fracture resistance. Experiments on $\{110\}$ plates tested in tension to fracture $\{111\}$ planes [104], and $\{001\}$ beams tested in bending to fracture $\{110\}$ planes [105], Fig. 4, show that cracks propagate with velocities of $\sim$1–3.5 km s^{-1} at crack driving forces of $\sim$2–17 J m^{-2}. There is an apparent “velocity gap” between 0 and $\sim$1 km s^{-1} for crack driving forces just exceeding the fracture resistance, $\sim$2 J m^{-2}, and at large crack driving forces the velocities approach an apparent upper limit of approximately 3/4 the Rayleigh wave speed, $v_R \sim 4.5$ km s^{-1} in Si. Atomistic fracture simulations using a range of potentials and boundary conditions [106–108] are in agreement with the experiments and show that the additional energy flux to the crack tip region (above the fracture resistance) during dynamic steady-state propagation is dissipated in the production of characteristic phonons. This process may be performed in reverse: shock loading of Si with laser-generated surface acoustic waves has been used to generate stress pulses leading to surface fracture [109–110]. Tests on $\{111\}$, $\{110\}$ and $\{100\}$ wafers generated 100 μm-scale cracks, following the major cleavage planes and extending $\sim$10 μm into the surface. The stresses reported for the formation of these cracks were 0.8 and 1.6 GPa, consistent with the strength values discussed above for wafers. Strong anisotropy was observed in the crack formation relative to the direction of propagation of the stress pulse, consistent with quasi-static simulations [111] considering crack propagation directional anisotropy on a cleavage plane. Such quasi-static simulations have also been applied to fracture at sharp notch tips in MEMS elements [112], illustrating the considerable over-loading required to initiate a crack.

The simulations suggest that the fracture surfaces formed under dynamic conditions are not atomically smooth, i.e., they are not perfect cleavage planes. Thermal fluctuations in the crack tip structure at large driving forces destabilise the steady-state propagation, leading to the formation of small branches in the crack front, dislocations and small, transient perturbations in the crack plane [106–108], the latter observable by scanning force microscopy [104]. Large, visible, features on the fracture surfaces of Si crystals, presumably arising from the growth of these small perturbations, have been known for some time: Cleavage steps are formed by the linking of parallel, but not coplanar, segments of a crack surface [113, 114] and such deflections and steps can be deliberately induced by interactions between a dynamically propagating crack and pre-existing dislocations inserted by prior high temperature deformation [105, 115]. Mirror, mist and hackle zones form sequentially as a crack propagates by deflections of the crack plane at length scales less than, approximately equal to, and larger than the wavelength of light, respectively [69, 116, 117]. Crack branching occurs after the hackle zone [69]. The surface roughness formed in the mist and hackle zones in Si can be quantified by a power-law dependency of the increased surface area on the length scale used to measure the area [69, 115]. The exponent can thus be interpreted as a “fractal” dimension that does appear to correlate with toughness. Although surface features are formed by dynamic fracture after the strength of a component has been exceeded, they do reflect conditions at the point of instability: fractography of cleavage steps and mirror-mist and mist-hackle boundaries has been used as a method for determining the failure location and possible loading conditions of Si strength test specimens [51, 52, 54, 66–71, 80, 82, 87, 105, 116] and wafers and dice [118, 119].

This overview provides compelling evidence that the fracture strength of Si is well understood qualitatively over a wide range of length scales. The degradation in the attainable strengths, from 10 GPa or more for MEMS elements with etching flaws to 100 MPa or less for wafers and dice with strength-limiting grinding or dicing flaws, is consistent with manufacturing processes optimised for characteristic scales of 1 μm to 300 mm, respectively. However, detailed, quantitative formulations of strength that provide clear linkages between the agents of flaw creation, the flaw scale and the resultant strength are absent. This is particularly so in the small strength range pertaining to wafers and dice, where the greatest Si manufactur-

ing yield and reliability concerns exist. Explicit connections between sharp contact load and geometry, crack size and strength for the commercially dominant (001)[110] orientation—required for process design, quality control and failure analysis—do not exist. Although the fracture anisotropy of Si is well accepted, it is not known whether this has any effect on the strengths of components containing sharp contact flaws remnant from grinding and dicing. The surface behavior of Si in HF solutions is well understood, but it is not known whether these reactive environments affect strengths by stress-corrosion cracking mechanisms during etching and cleaning. The effects of doping on dislocation mobility and diffusion in Si are well studied and although it would appear unlikely, it is not known whether doping affects fracture strengths. The following sections address these issues in an extensive experimental study based on controlled-flaw indentation techniques developed previously [26]. As well as providing answers to practical questions associated with Si manufacturing, parameters required to estimate fundamental properties, such as toughness, are determined.

3. Experimental details

3.1. Materials

The primary test vehicles were (001) discs of single crystal Si, 35 mm diameter × 3 mm thickness. The (001) faces, perpendicular to the disc axis, were polished; a small (110) flat was ground on the edge of the discs, parallel to the axis, Fig. 6a. Three doping levels were used: heavily P-doped *n*-type, electrical resistivity 5–15 mΩ cm; heavily B-doped *p*-type, resistivity 5–15 mΩ cm; and undoped intrinsic, resistivity > 20 Ω cm. The large, degenerate, doping levels were chosen to allow the effects of doping on fracture behavior to be examined. The samples were tested as discs or cut by diamond saw into 6 mm wide bars perpendicular to the (110) flat, Fig. 6a. Except for the dimensions, this is the semiconductor-industry standard geometry with two, secondary, orthogonal {110} cleavage planes perpendicular to the (001) surface and four, primary {111} cleavage planes at 54.5° to the (001) surface, intersecting along orthogonal <110> traces in the (001) plane, Fig. 4b. Some samples were cut into bars at 45° to the (110) flat, perpendicular to the (100) plane, Fig. 6b.

The secondary test vehicles were ($\bar{1}$ 10) discs of single crystal Si, 100 mm diameter × 2.5 mm thickness. The ($\bar{1}$ 10) faces, perpendicular to the disc axis, were polished; a small (111) flat was ground on the edge of the discs, parallel to the axis. The discs were lightly P-doped *n*-type with resistivity 5 Ω cm. This disc geometry has two, primary {111} cleavage planes perpendicular to the ($\bar{1}$ 10) surface intersecting at 109° along in the ($\bar{1}$ 10) surface, and two additional {111} cleavage planes at 70.9° to the ($\bar{1}$ 10) surface intersecting along a <110> trace in the surface.

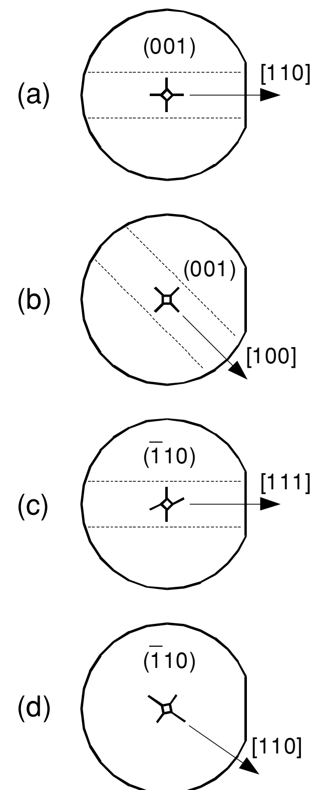

Figure 6 Schematic diagrams illustrating the wafer and flat geometry and Vickers indentation alignments used here on Si. (a) The predominant (001)[110] semiconductor processing and fracture geometry; indentation onto the (001) plane with the diagonal aligned along the [110] direction, allowing for easy (110) cleavage. (b) Pathological (001)[100] alignment, leading to poor (100) cleavage; (c) The ($\bar{1}$10)[111] alignment used in fundamental studies of the primary (111) cleavage; and (d) An alternative ($\bar{1}$10)[110] alignment, used to generate (110) and (100) cleavage. Dotted lines indicate the orientation of bars cut from the wafers for uniaxial strength testing.

The discs were cut into bars 6 mm wide, perpendicular to the (111) flat, such that a tensile test would cleave the bar along the primary cleavage plane, Fig. 6c.

The tertiary test vehicles were discs of polycrystalline Si, 35 mm diameter × 3 mm thickness. The faces perpendicular to the disc axis were polished. The grain size of the material varied from approximately 100 μm in the central 5 mm of the disc to 2 mm at the disc periphery.

3.2. Indentation tests

The polished faces of the discs were indented with a Vickers diamond pyramid in air using loads, *P*, in the range 0.1 to 300 N, generating controlled contact flaws consisting of remnant plastic square contact impressions, half-penny cracks and lateral cracks, Fig. 1. Indentations were performed under two conditions. In the first, using a custom-built instrument under displacement control in air [32], the indentation load, *P*, and displacement, *h*, were monitored during the load-unload contact cycle to generate the hys-

teretic *P-h* response of the material as a function of peak load in the range 5 to 80 N, Fig. 5a. Compliance of the instrument and unclamped specimens was estimated by comparison with calibrated responses on a similar instrument [120, 121]. In the second, using dead-weight gravity loading in air (Zwick 3212, Zwick USA, Kennesaw, GA; Buehler 2103, Buehler Ltd, Lake Bluff, IL), Fig. 5b, the size of the residual contact impression semi-diagonal a and the lengths of surface traces of the half-penny cracks c_1 were measured after indentation as a function of peak load 0.1 to 300 N. Indentions were made at various orientations, designated by the indenting plane, followed by the orientation of the indenter diagonal, (*hkl*)[*uvw*], such that fracture plane of interest is (*uvw*), Fig. 6; the conventional microelectronics orientation is (001)[110], Figs 1 and 6a, and the conventional dynamic fracture orientation is $(\bar{1}10)[111]$, Fig. 6c. The polycrystalline discs were indented in the fine-grained center.

3.3. Inert strength tests

The maximum sustainable applied stress, or inert strength, σ_{max}, was measured for disc and bar specimens containing indentation flaws in the load range 0.1 N to 300 N.

Indentations were placed in the center of the (001) discs in either the (001)[110] or (001)[100] orientations. The discs were then stressed in flat-on-three-ball biaxial flexure with the indented face in tension, using a 32 mm diameter for the outer circle of the three-ball support and a 4 mm diameter for the inner flat. Loading to failure occurred in 50 ms or less, with load monitored using a piezoelectric load cell and peak load converted to the applied outer-fiber failure stress σ_{max} using standard plate theory [122], Fig. 5c. The applied stressing rate to failure was approximately 5 GPa s^{-1}. No difference in strength was observed at this stressing rate for tests in air or for tests in which the indentation was covered with silicone oil (to further impede the diffusion of moisture to the crack tip during testing). The tests were therefore regarded as "inert" (at least for Si) and the majority of tests were performed in air.

For bars cut from the $(\bar{1}10)$ discs, indentations were placed in the center of the bar in the $(\bar{1}10)[111]$ orientation. The bars were then stressed in four-point uniaxial flexure with the indented face in tension, using a 30 mm outer span and a 7.5 mm inner span, using a stiff, displacement-controlled loading frame. Loading to failure occurred in 10 s or less, with load monitored using a conventional resistance load cell and peak load converted to the applied outer-fiber failure stress σ_{max} using standard beam theory [122].

3.4. Crack propagation tests

The stable propagation of indentation cracks under the influence of applied stress was measured in air using a custom built instrument [123] similar to those used earlier [26, 73]. Single indentation flaws were generated in the centers of the (001)[110] and (001)[100] bar specimens over the load range 2 N to 50 N, Figs 6a and b. The bars were then stressed in four-point uniaxial flexure with the indented face in tension, using a 30 mm outer span and a 7.5 mm inner span, using a stiff, displacement-controlled loading fixture mounted on an inverted optical microscope, Fig. 5d. The length c of the indentation cracks perpendicular to the stressed direction was monitored throughout the test, along with load—converted to the applied outer-fiber stress σ_a via standard beam theory. Load was increased in small increments after crack motion had ceased at each load level, thereby generating the stable $\sigma_a(c)$ trajectory for equilibrium indentation crack propagation for Si in air.

3.5. Reactive strength tests

The failure stress, or reactive strength σ_f, of disc specimens containing indentation flaws was measured in two ways.

In the first, the specimen was indented in air using a fixed indentation load of 2 N, followed by applied stressing to failure while exposing the indentation to either distilled water (pH = 7) or to an aqueous solution of NH_4-buffered 0.1 M HF (BHF, pH = 4.5)[102], Fig. 5f. Failure stress was measured over the applied stressing-rate range of 5×10^{-3} MPa s^{-1} to 5×10^{3} MPa s^{-1}, using the resistance load cell to monitor load for tests longer than 10 s and the piezoelectric load cell for shorter tests.

In the second test, the specimen was indented in air as before and then immersed in either the water or BHF for zero-stress-aging exposure times of 1 s to 24 h. The specimen was then rinsed in water, hot-air dried, and an inert strength test conducted, undergoing the sequence in Figs 5b-e-c. In this way, the effects on flaws—and consequent strengths—of exposure to reactive environment alone could be distinguished from the effects of exposure+stress.

4. Results and analysis

4.1. Indentation deformation

The driving force for half-penny crack and lateral crack initiation at a sharp contact impression is the residual stress field deriving from the strain mismatch effects of the localized plastically-deformed zone immediately beneath the contact impression imbedded in the surrounding elastically-strained matrix [25]. The elastic-plastic nature of the sharp contact process was characterized by load-displacement measurements during indentation. Fig. 7 shows representative load-displacement measurements for single crystal (001)[110] and polycrystalline in-

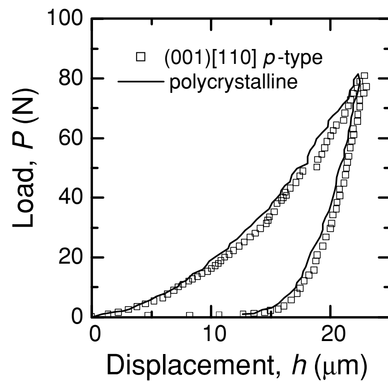

Figure 7 Indentation load-displacement, *P-h*, behavior during Vickers indentation of (001)[110] single crystal and polycrystalline Si.

dentations to a peak load of 80 N. The traces are hysteretic, indicative of the combined effects of elastic+plastic deformation during loading and elastic recovery alone during unloading (∼45% axial recovery is typical for Si [13, 121]). The traces are also somewhat erratic, indicating discrete events taking place during the indentation contact—likely the formation and slippage of shear faults—events not usually observed at small loads using load-controlled "nanoindenters" [13] or here at small loads. The peak contact depth, h_{max}, increased with peak contact load, P, as shown in Fig. 8. During loading of a geometrically-similar indenter, load is quadratically related to displacement [10, 24], to give at peak load

$$h_{max} = f_L P^{1/2} \quad (6)$$

where f_L is a function of the modulus and hardness of the material and the geometry of the indenter. The h_{max} data are consistent this relationship and with other observations [120, 121] in the same load range and extrapolation into the sub-μm nanoindentation range [13, 121]. Also consistent with previous observations [13], and as suggested by Fig. 7, there was no apparent difference between the indentation load-displacement behavior of the three (001) Si variants or the polycrystalline Si at any load.

The residual indentation geometry of Si, however, was observed to be extremely load-dependent, as indicated in the micrograph series of Fig. 9, which shows (001)[110] indentations. Over the load range $P = 0.5$ N to 20 N, the indentation pattern increased in size and changed from a "classic" geometry of a square contact impression with four half-penny surface crack traces colinear with the impression diagonals emanating from the impression corners, Fig. 9a, to one dominated by the removal of surface material by shallow lateral cracks emanating from the impression edges, Fig. 9f. A similar transition in behavior was observed over the same load range for $(\bar{1}10)[110]$ indentations and on the polycrystalline material. No features could be identified in the load-displacement traces

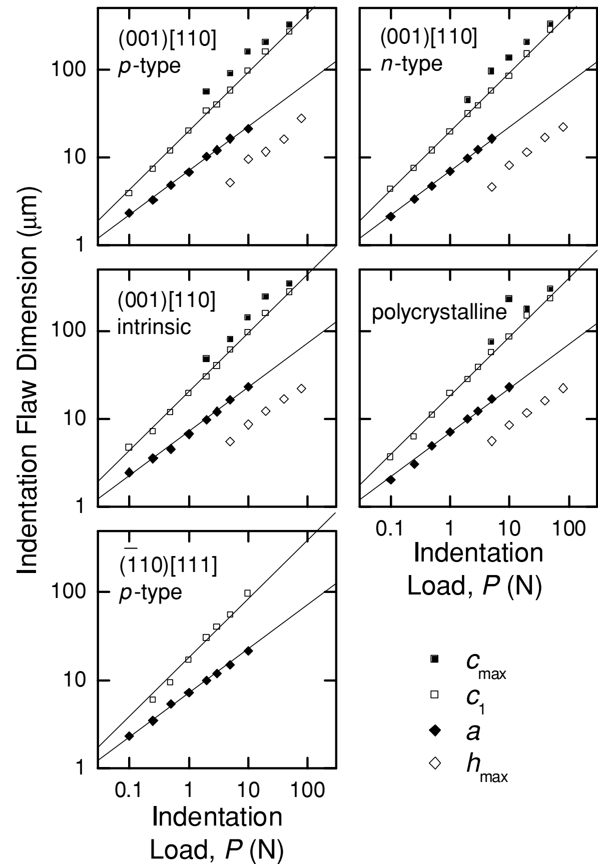

Figure 8 Plots of Vickers indentation deformation and fracture parameters for Si as a function of indentation load, P: maximum axial contact displacement during indentation, h_{max}; residual transverse contact impression dimension, a; post-indentation half-penny crack length, c_1; and instability crack length during stressing, c_{min}. Symbols for contact displacement represent individual measurements at each load. Symbols for contact impression and post-indentation crack length data represent the means of measurements on three-four indentations. Symbols for instability crack length represent the means of measurements of four cracks. Standard deviation limits for the last three cases are approximately the symbol size. The solid lines are best fits consistent with constant hardness and toughness, Equations 7 and 12.

and associated with subsequent observations of fracture damage, similar to observations on ceramic materials [32, 120, 121]. However, it is suspected that the almost-zero load, large displacement recoveries observed during the final stages of unloading from large peak loads (e.g., the *p*-type material in Fig. 7) were indicative of unloading of extremely compliant lateral cracks [124].

Striking as the fracture damage in Fig. 9 is, the energy dissipated during indentation contact goes primarily into plastic deformation, which appears as a residual contact, or "hardness," impression. The mean supported contact pressure or hardness H can be estimated from residual contact impression dimensions by assuming that transverse dimensions do not recover during unloading. For Vickers indentations these are assumed to be the impression diagonals to give the projected contact area as $2a^2$, where a is the contact impression semi-diagonal, such that

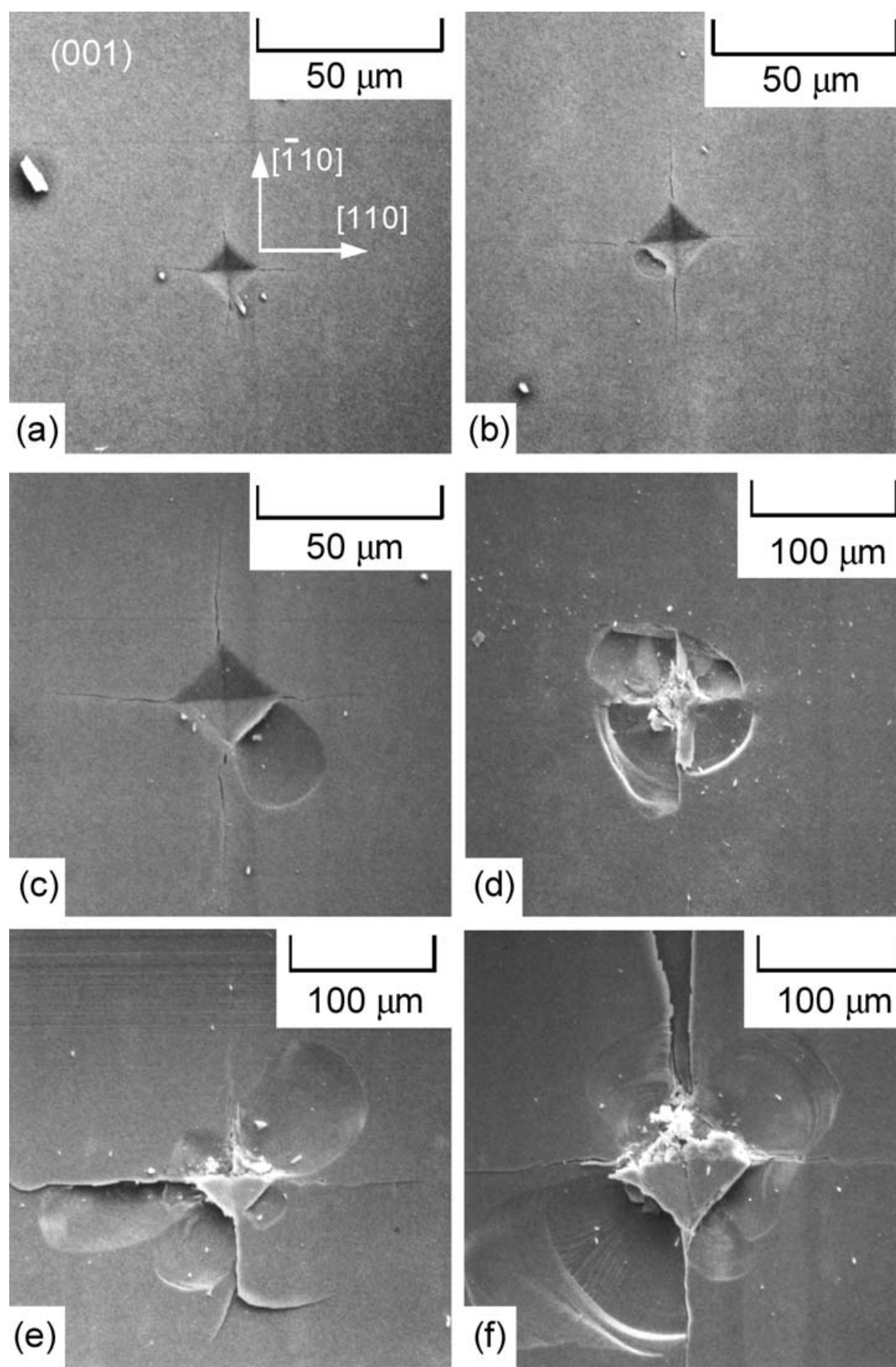

Figure 9 Scanning electron micrographs of (001)[110] Vickers indentations in *n*-type Si, illustrating the increasing lateral cracking and chipping with increasing indentation load, *P*: (a) 0.5 N; (b) 1 N; (c) 2 N; (d) 5 N; (e) 10 N; and (f) 20 N.

the hardness is $H = P/2a^2$ and

$$a = (P/2H)^{1/2}. \qquad (7)$$

Fig. 8 shows the impression dimension a as a function of indentation load P over the load range 0.1 N to 10 N (as shown in Fig. 9, larger loads generated residual contact damage that did not allow unambiguous indentation dimension measurements). In agreement with Equation 7, the impression dimension data follow a $P^{1/2}$ dependence over the load range tested, as indicated by the best-fit lines of slope $\frac{1}{2}$ (in logarithmic coordinates). The hardness values characterizing this behavior are given in Table II and show no significant difference in behavior between the Si

TABLE II Vickers indentation contact properties of silicon

Indentation orientation, (Plane) [Diagonal]	Doping	Hardness, H (GPa)	Half-Penny crack parameter, $P/c_1^{3/2}$ (MPa m$^{1/2}$)	Total/contact displacement ratio, β
Present work	*p*-type	10.4 ± 0.9	11.5 ± 1.0	1.29 ± 0.16
{001}<110>	*n*-type	10.4 ± 0.6	11.7 ± 0.8	1.16 ± 0.11
	Intrinsic	10.1 ± 1.2	11.3 ± 1.0	1.21 ± 0.06
polycrystalline	–	10.5 ± 1.5	13.1 ± 1.5	1.22 ± 0.04
{001}<100>	*n*-type	–	$\sim$27	
{110}<111>	*p*-type	10.1 ± 0.8	13.6 ± 2.7	
{110}<110>	*p*-type	9.4 ± 0.7	9.5 ± 0.9	
{110}<100>	*p*-type	9.4 ± 0.7	16.7 ± 2.2	
Lawn *et al.* [26]				
{111}<random>	Unknown	9.0	12.5 ± 1.8	
Tsai and Mecholsky [116]				
{001}<110>	Unknown		10.8 ± 2.2	
Ebrahimi and Kalwani [125]				
{001}<110>	Unknown	13.3 ± 1.2	11.5 ± 0.8	
{001}<100>		13.6 ± 1.1	$\sim$20	
{110}<111>		12.4 ± 0.8	13.0 ± 0.9	
{110}<110>		11.2 ± 0.7	8.9 ± 0.7	
{110}<100>		12.3 ± 1.0	15.2 ± 1.3	
{111}<110>		10.0 ± 0.8	11.6 ± 1.0	
Fancher *et al.* [126]				
polycrystalline	Intrinsic	9.6 ± 1.8	11.7	
Swadener and Nastasi [127]				
{001}<110>	*p*-type	13.5 ± 0.5	12.4 ± 1.6	
	n-type (P)	13.5 ± 0.5	13.4 ± 1.8	
	n-type (Sb)	13.5 ± 0.5	13.3 ± 1.8	

variants. The values reported here ($\sim$10 GPa) are in the middle of the range reported or determined from other observations (9–13.5 GPa) [26, 116, 125–127] using the same indentation load range. Inspection of Table II shows that there is no effect of doping on Si hardness, but that a possible but small trend $H_{(001)} > H_{(110)} > H_{(111)}$ could exist.

An estimate of the indentation recovery external to the contact impression may be made from the displacement ratio $\beta = h_{\max}/h_c$ [32, 120], where h_c is the contacted depth at peak load given by

$$h_c = a \cot \phi \tag{8}$$

and $2\phi = 146^\circ$ is the included edge angle of the (Vickers) indenter. Using the data in Fig. 8 and Equations 7 and 8, the depth recovery ratio over the load range $P = 5$ N to 80 N was estimated as $\beta \sim 1.22$ for the three (001) and polycrystalline materials, Table II. This suggests that exterior recovery, $\beta - 1$, was about half of the total recovery observed during indentation; the remainder must have occurred interior to the contact impression. This β value for Si is intermediate to that of soda-lime glass ($\sim$1.1) and sapphire ($\sim$1.8) [120], suggesting that β increases with material *E/H* ratio and that Si should exhibit a large "residual" stress field associated with the elastic-plastic mismatch between the deformation zone and the surrounding matrix [25, 32].

4.2. Indentation fracture

The partial recovery, $1 \leq \beta \leq 2$, of the contact impression is an indication of the residual stress field surrounding the contact impression after indenter removal. Half-penny and lateral crack development at indentations—although influenced by the recovered elastic contact field—is dominated by this residual field [25, 32, 72, 73, 124]. For well-developed cracks (operationally, about a factor of two larger than the contact impression) the residual field is well modeled by outward, point-force loading at the impression center, with compensation for free-surface effects. The residual stress-intensity factor, K_r, driving the half-penny cracks is then given by [25]

$$K_r = \chi P / c^{3/2} \tag{9}$$

where the dimensionless amplitude χ is given by

$$\chi = \xi (E/H)^{1/2} \tag{10}$$

and the elastic-plastic nature of the contact is reflected in the E/H term and ξ characterizes the geometry of the impression-crack system. The geometry factor ξ takes a maximum value of ξ_0 in the absence of any mechanisms that either relax the residual stress field or geometrically interfere with the propagation of the half-penny cracks. Critically for Si, lateral cracks provide such a mechanism [26, 124, 128–131], decoupling the plastic deformation zone from the matrix and truncating the surface traces of

the half-penny cracks (Fig. 9), thereby reducing χ from its maximum value of χ_0, particularly during the latter stages of unloading at large indentation loads [32].

The residual stress-intensity factor characterizes a stabilizing crack propagation field, leading to stable equilibrium lengths for the half-penny cracks defined by the equilibrium criterion of

$$K_r = T, \tag{11}$$

where T is the material toughness. Under "ideal" conditions, in which the residual stress field is unrelaxed and the environment is inert, the stable equilibrium half-penny crack length is given by

$$c_0 = (\chi_o P/T_0)^{2/3}, \tag{12a}$$

where T_0 is the maximum value of the toughness appropriate to an inert, unreactive environment. The stable equilibrium crack length in a reactive (moist) air environment is then given by

$$c_1 = (\chi_0 P/T_{air})^{2/3} \geq c_0, \tag{12b}$$

where $T_{air} = T_0$ is the reduced value of the toughness appropriate to air (this is not expected to be a large effect in Si), which is further modified by the effects of residual field reduction to

$$c_2 = (\chi P/T_{air})^{2/3} \leq c_1, \tag{12c}$$

where $\chi \leq \chi_0$ is the reduced value of the amplitude term in the presence of lateral cracks (this is expected to be a large effect in Si). Usually the relationship $c_0 \leq c_2 \leq c_1$ is observed and that as lateral cracking occurs during unloading, after the attainment of the full half-penny crack length, the half-penny cracks stay metastably trapped $K(c_1) > T$ at the longer length of c_1, and this is the crack length that is observed. (Nevertheless, it is the fictitious initial crack length c_2 that determines behavior during crack propagation in reactive environments.) Analogously, there is yet another fictitious initial crack length that determines behavior in inert environments,

$$c_3 = (\chi P/T_0)^{2/3} \leq c_2, \tag{12d}$$

and hence inert strengths.

Fig. 8 shows the half-penny surface trace dimension c_1 as a function of indentation load P over the load range 0.1 N to 50 N. In agreement with Equation 12b, the crack-length data follow a $P^{2/3}$ dependence over the load range tested, as indicated by the best-fit lines of slope 2/3. The $P/c_1^{3/2}$ values characterizing this behavior are given in Table II and show no significant difference in behavior between the three doping levels for (001)[110] indentations and quantitative consistency with some [116, 125], but not all [127] previous observations. The latter study also claimed an effect of doping, but others [132], in agreement with the data here do not. Also consistent with previous observations was a strong indentation anisotropy in the (001) plane [125]. This is illustrated in Fig. 10, which shows the change in residual damage as the indentation is rotated from (001)[110] to (001)[100], Fig. 6a, b; the traces of the half-penny cracks decreased in length and exhibited curvature and deflections back towards the ⟨110⟩ traces, lateral cracking and chipping become more prevalent, obscuring or removing both the contact impression and any half-penny crack traces, to leave only an impact crater with very short half-penny cracks and thus very large $P/c_1^{3/2}$ values. A more clearly measurable indentation anisotropy was observed in the (110) plane, as illustrated in Fig. 11, which shows the change in residual damage as the indentation is rotated from $(\bar{1}10)[111]$ to $(\bar{1}10)[110]$, Fig. 6c, d; lateral cracking and chipping became somewhat more prevalent at intermediate orientations. However, the greatest effect was that the cracks with ⟨112⟩ traces in the starting orientation exhibited intermediate lengths to those with shorter [001] and longer [110] traces in the final orientation. This effect, and the longer crack lengths (larger $P/c_1^{3/2}$ values) for (001)[110] cracks relative to $(\bar{1}10)[111]$ cracks has also been observed previously [125]. Overall, however, indentation anisotropy of Si is fairly weak and a $P/c_1^{3/2}$ value of 11–12 MPa $m^{1/2}$ appears typical for most surface and indenter orientations.

The slope-2/3 trend observed in Fig. 8 for the half-penny crack lengths suggests an invariant value of χ_0 [Equation 12b, as the cleavage toughness T_{air} is invariant] at the point in the indentation cycle at which the half-penny crack lengths were established—at least over the indentation load range examined. The strong increase in the visible lateral cracking and chipping in Figs 9 and 10 suggests that the reduction to χ on lateral crack initiation and growth subsequent to half-penny formation should thus be strongly load or orientation dependent. However, careful optical microscope observations of (001)[110] indentations revealed that there was visible surface uplift associated with lateral cracks in all four indentation quadrants over the complete indentation load range and that the increase in indentation load from 0.1 N to 300 N simply increased the number of quadrants in which material was removed. Previous studies of lateral crack influences on indentation half-penny and radial crack lengths [129, 130] have shown that the formation of lateral cracks is much more important than subsequent removal of material in reducing the residual field intensity. Hence, as lateral cracks were observed over the entire load range here, only a small variation in the post-indentation value of χ with load is expected (changes in orientation alter the

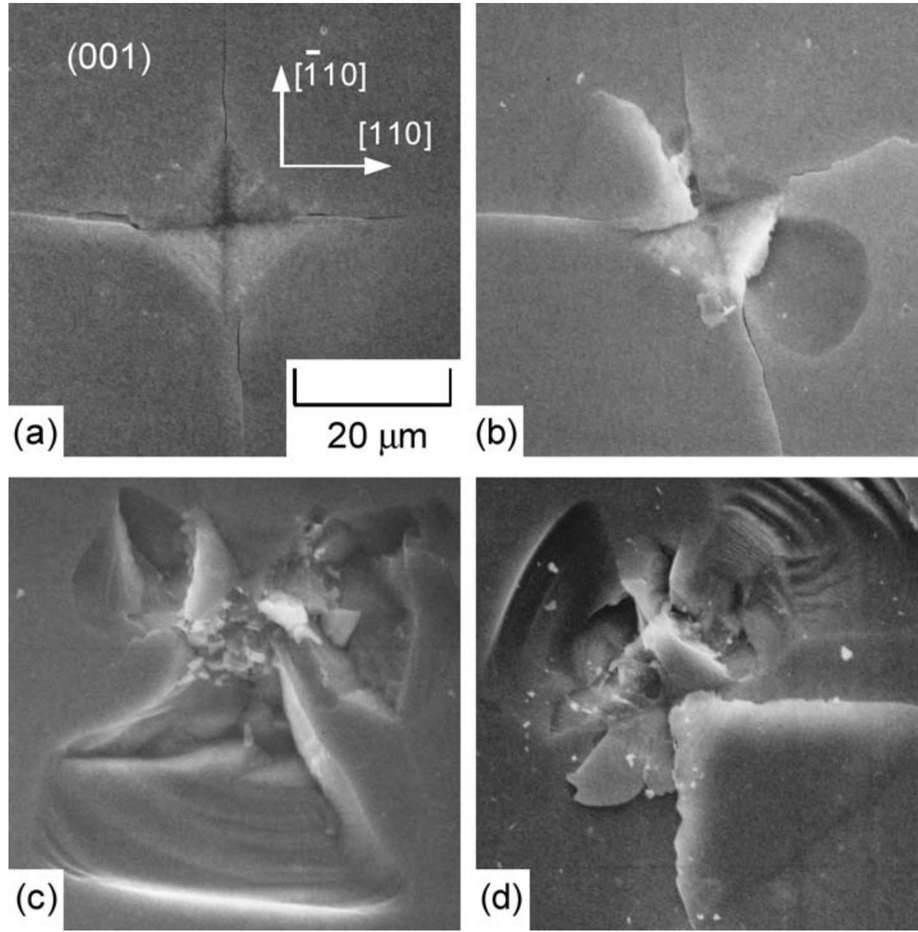

Figure 10 Scanning electron micrographs of 2 N Vickers indentations in *p*-type Si, illustrating the increasing lateral cracking and chipping with increasing misorientation from the (001)[110] geometry shown in (a): (b) 15° misorientation; (c) 30° misorientation; and (d) 45° misorientation, (001)[100].

fundamental indentation geometry and could have much greater effects).

4.3. Inert strength

A globally-applied uniform stress σ_a acting on a semi-circular crack of radius c imposes a stress-intensity factor of

$$K_a = \psi\sigma_a c^{1/2}, \tag{13}$$

where ψ is a dimensionless (amplitude) geometry term. $K_a(c)$ is a destabilizing field as $dK_a/dc>0$ and therefore acts to propagate a crack away from an equilibrium position, as opposed to the stabilizing nature of the $K_r(c)$field, for which $dK_r/dc<0$. When superposed on the residual stress-intensity factor of the indentation contact field, the equilibrium condition becomes

$$K = K_a + K_r = T \tag{14}$$

where K is the net stress-intensity factor. Under inert conditions, $T = T_0$, and the onset of instability (and thus dynamic fracture) for an indentation crack is specified by the simultaneous solution of the equilibrium condition of Equation 14 and the global destabilizing condition of $dK/dc \geq 0$. The crack length and applied stress at the instability point are [73]

$$c_{max} = \left(\frac{4\chi P}{T_0}\right)^{2/3} = 4^{2/3}c_3 \cong 2.52c_3 \tag{15a}$$

$$\sigma_{max} = \frac{3T_0}{4\psi c_{max}^{1/2}} = \frac{3T_0^{4/3}}{4^{4/3}\psi\chi^{1/3}P^{1/3}} \tag{15b}$$

where the subscript "max" indicates that this is the maximum sustainable stress—or inert strength—of a material containing an indentation flaw. A key feature of this formulation is that the initial crack length does not appear explicitly in the expression for the inert strength, Equation 15b. Provided the condition $c_1 \leq c_{max}$ is met, the inert strength is invariant with respect to the initial crack

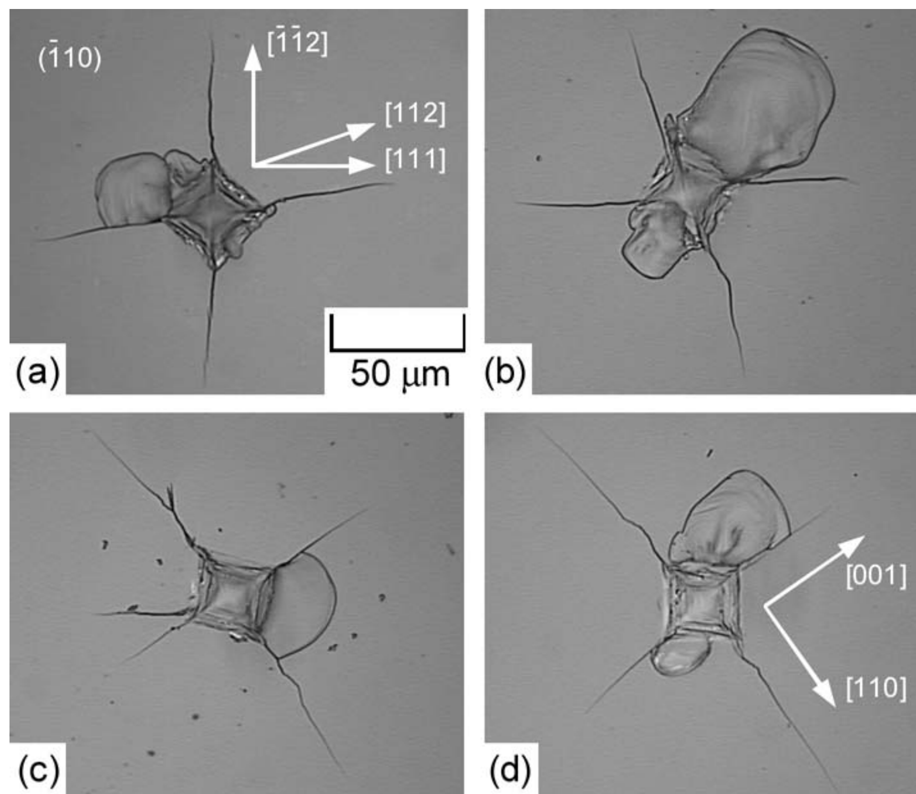

Figure 11 Optical micrographs of 2 N Vickers indentations in *p*-type Si, illustrating the intermediate increase in lateral cracking and chipping on increasing misorientation from the ($\bar{1}$ 10)[111] geometry shown in (a): (b) ∼10° misorientation; (c) ∼20° misorientation; and (d) ∼35° misorientation, ($\bar{1}$ 10)[110].

length. Consistent with this invariance is that it is the reduced value of χ active during application of the stress that appears, not the peak value χ_0, active during crack formation. The reduction in χ due to decreased constraint on the plastic deformation zone by increased lateral cracking at large indentation loads is described by [128, 131]

$$\chi = \chi_0/(1 + P/P_L), \qquad (16)$$

where P_L is an empirically-determined characteristic load. Combining Equations 15 and 16 shows that P_L divides the strength behavior into the ideal, indentation load-controlled asymptote,

$$\sigma^P_{max} = \frac{3T_0^{4/3}}{4^{4/3}\psi\chi_0^{1/3}P^{1/3}}, \quad P \ll P_L \qquad (17a)$$

and the invariant, lateral crack-controlled asymptote,

$$\sigma^L_{max} = \frac{3T_0^{4/3}}{4^{4/3}\psi\chi_0^{1/3}P_L^{1/3}}, \quad P \gg P_L. \qquad (17b)$$

A convenient general expression for inert strength as a function of indentation load is then

$$\sigma_{max} = \sigma^L_{max}(1 + P_L/P)^{1/3} \qquad (18)$$

Fig. 12 shows the inert strength σ_{max} as a function of indentation load P over the range 0.1–300 N. The solid lines are best fits of Equation 18 to the data and dashed lines represent the asymptotes of Equation 17. The strength data are well described by a decrease in χ associated with lateral cracking at large indentation loads; the measured strengths at the largest loads for the (001) Si variants are about a factor of two greater than the values extrapolated from the small load ideal variation asymptotes. The values of P_L, σ^L_{max} and $\sigma^L_{max}P_L^{1/3}$ characterising the fits are given in Table III, along with some values inferred from previous observations [16, 74, 75, 116]; a composite plot of the responses over the range of the measurements is shown in Fig. 13. Consistent with the crack length measurements, no significant difference in strength behavior of the (001)[110] variants as a function of doping was observed. Furthermore, the parameter $\sigma^L_{max}P_L^{1/3} = \sigma^P_{max}P^{1/3}$, characterising the small indentation load strength and proportional to the toughness (Equation 17) was not significantly different for any of the materials, falling at the low end of the 120–160 MPa $N^{1/3}$ range observed previously. Also consistent with the crack length measurements was the small variation in χ over most of the indentation load range: P_L values characterising the onset of deviation from the ideal strength response were large relative to the range used for the crack length measurements, particularly so for the poly-

TABLE III Vickers indentation fracture strength properties of silicon

Indentation orientation, (Plane) [Diagonal]	Doping	Characteristic indentation load, P_L (N)	Characteristic strength, σ^L_{max} (MPa)	Indentation strength parameter, $\sigma^L_{max} P_L^{1/3}$ (MPa N1/3)
Present work	p-type	19.0 ± 2.7	47.1 ± 4.0	125.7 ± 3.1
(001)[110]	n-type	20.1 ± 5.2	48.8 ± 7.6	132.7 ± 5.8
	Intrinsic	29.8 ± 7.8	43.2 ± 6.8	134.1 ± 5.5
polycrystalline		77.8 ± 22.9	29.5 ± 5.1	125.8 ± 4.3
$(\bar{1}\,10)[111]$	p-type	100.5 ± 36.8	31.8 ± 6.8	147.8 ± 6.0
Lawn *et al.*[26]				
{111}<random>	Unknown			$\sim 130 \pm 13$
Tsai and Mecholsky [116]				
(001)[110]	Unknown			162 ± 38
Pajares *et al.* [74]				
{100}<010>	Unknown			$\sim 140 \pm 20$ (B)
Jung *et al.* [75]				
{111}<random>	Unknown			$\sim 120 \pm 15$ (B)

B: Berkovich indenter (three-sided, same equivalent-cone included angle as four-sided Vickers).

crystalline and $(\bar{1}\,10)[111]$ materials. Close examination of the large load region for all materials shows that the fits tend to overestimate the data. This suggests that at the largest loads, the reduction in χ and consequent reduction in c_{max} (Equation 17a) voids the condition $c_1 \leq c_{max}$ required for precursor stable extension of the crack prior to failure, thus decreasing the strength from the maximum attainable value [26, 128] .

4.4. Crack propagation

Using Equations 9 and 13 in Equation 14 and inverting yields an equilibrium $\sigma_a(c)$ response:

$$\sigma_a = \frac{1}{\psi c^{1/2}}\left(T - \frac{\chi P}{c^{3/2}}\right) \tag{19}$$

Under inert conditions ($T = T_0$), this function has two zero minima: one at $c = c_3$ and one asymptote at $c \to \infty$. Between these two minima lies a maximum (also obtainable by solving another statement of the instability condition, $d\sigma_a/dc = 0$) at c_{max}, σ_{max} (Equation 15). An analogous calculation under reactive equilibrium conditions in air ($T = T_{air}$) yields

$$c_{min} = \left(\frac{4\chi P}{T_{air}}\right)^{2/3} = 4^{2/3} c_2 \cong 2.52 c_2 \tag{20a}$$

$$\sigma_{min} = \frac{3T_{air}}{4\psi c_{min}^{1/2}} = \frac{3T_{air}^{4/3}}{4^{4/3}\psi \chi^{1/3} P^{1/3}} \tag{20b}$$

where the subscript "min" indicates that this is the minimum sustainable stress—or reactive strength—of a material containing such a flaw. σ_{max} and σ_{min} are not expected to be too different, if at all, in Si The crack lengths at equilibrium instability under the action of applied stress are related to the zero-stress, initial crack length by

$$c_{min} = 4^{2/3} (\chi/\chi_0)^{2/3} c_1 \tag{21a}$$

and

$$c_{max} = 4^{2/3} (T_{air}/T_0)^{2/3} (\chi/\chi_0)^{2/3} c_1. \tag{21b}$$

These relations are important as they dictate the degree of metastable trapping of cracks at longer lengths relative to ideal $\sigma_a(c)$ trajectories, due to lateral-crack mediated late- or post-indentation cycle χ reduction (Equation 21a) and environment-controlled post-indentation T increase (Equation 21b).

The behavior of the $\sigma_a(c)$ function, showing the effects of environment on the stable, metastable and unstable points is perhaps best studied by normalizing the applied stress, crack length and toughness by

$$S = \frac{\sigma_a}{\sigma_{min}} \qquad C = \frac{c}{c_{min}} \qquad \mathbf{T} = \frac{T}{T_{air}} \tag{22}$$

to yield Equation 19 as

$$S = \frac{4}{3C^{1/2}}\left(\mathbf{T} - \frac{1}{4C^{3/2}}\right), \tag{23}$$

which for $\mathbf{T} = 1$ has zeroes at $C_2 = 4^{-2/3}$ and $C \to \infty$ and a maximum at $C = 1$, $S = 1$ as shown in Fig. 14. (Although the system is under load control and thus stress is the independent variable in Equation 23, S is usually plotted on the ordinate in keeping with the convention that the extensive variable C be plotted on the abscissa.)

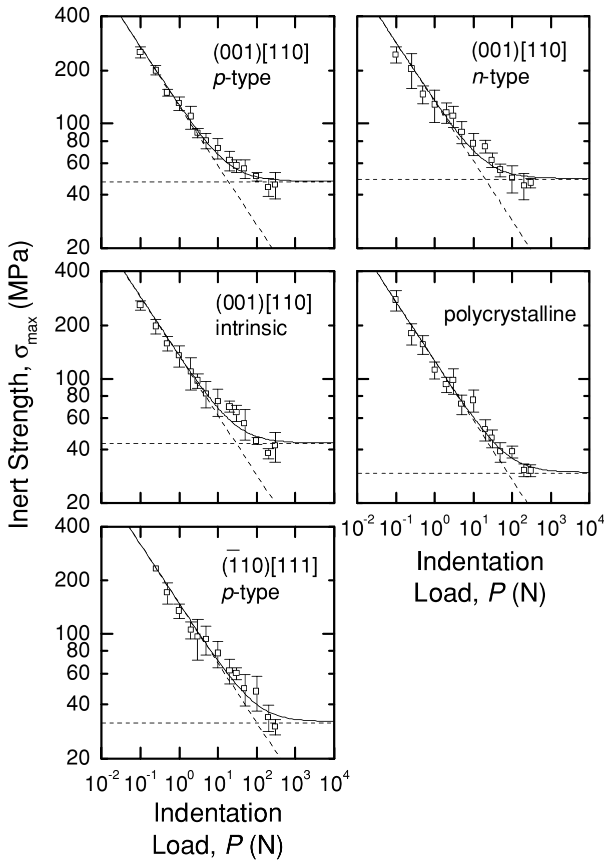

Figure 12 Plots of inert strength, $\sigma_{\max}$, as a function of indentation load, P, for Si. The symbols represent the means and standard deviation limits of at least five strength tests at each load; the (001)[110] and polycrystalline materials were biaxially stressed, the $(\bar{1}\,10)$ [111] material was uniaxially stressed. The solid lines are best fits consistent with lateral crack-mediated diminution of the residual contact field with increasing indentation load, Equation 18; the dashed lines are the small and large load asymptotic responses, Equation 17.

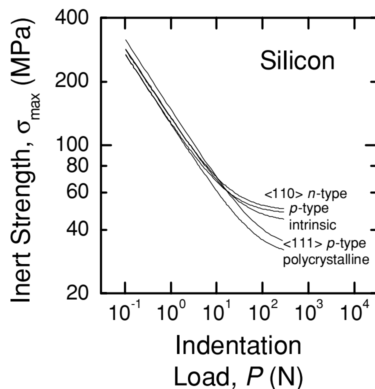

Figure 13 Composite plot of the inert strength responses of Si, allowing comparison of indentation orientation and fracture plane, (001)[110] vs $(\bar{1}\,10)$[111], doping, *n*- vs *p*-type vs intrinsic, and single crystal vs polycrystal. The solid lines are the best fits from Fig. 12, plotted over the range of the experimental observations. In the small indentation-load region there is no significant difference in strength.

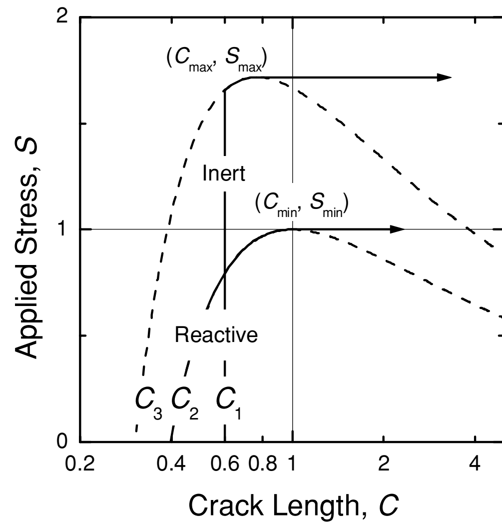

Figure 14 Plots of ideal equilibrium applied stress-crack length, *S-C*, trajectories—dashed lines, normalised coordinates—for indentation fracture in inert and reactive environments, from Equation 23. Post-indentation half-penny cracks in Si are metastably trapped at a crack length C_1, larger than either the reactive (C_2) or inert (C_3) zero-stress equilibrium lengths, leading to the truncated trajectories indicated by the solid lines.

The stable precursor extension of the indentation crack prior to failure is obvious in Fig. 14: Under ideal reactive conditions, the as-indented system begins at (C, S) = ($4^{-2/3}$, 0) and as the stress is increased moves along the stable branch of the $S(C)$ equilibrium trajectory, where $\mathrm{d}S/\mathrm{d}C > 0$, to eventually reach instability at (1, 1) where $\mathrm{d}S/\mathrm{d}C = 0$—the unstable branch, where $\mathrm{d}S/\mathrm{d}C < 0$, is not accessible—and failure proceeds along a horizontal trajectory of $S = 1$, $C \to \infty$. Under realistic (i.e., "non-ideal") reactive conditions, in which the failure process ensues from a metastable crack length of ($C_1 \geq C_2 = 4^{-2/3}$), the system begins at (C_1, 0) and as the stress is increased the system remains at the metastable crack length C_1 and proceeds along a vertical trajectory until the reactive equilibrium trajectory is reached whereat failure occurs as before. However, provided the condition $C_1 \leq 1$ is met, the failure conditions, and hence the reactive strength remain the same (i.e., the initial crack length does not matter).

Under inert conditions, $\mathbf{T} = \mathbf{T}_0 > 1$ and failure occurs at ($C_{\max}$, $S_{\max}$) = ($T_0^{-2/3}$, $T_0^{4/3}$). Provided the condition $C_1 \leq T_0^{-2/3}$ is met, failure under inert conditions proceeds as for non-ideal reactive conditions; the system begins at (C_1, 0) and proceeds with a vertical trajectory as the stress is increased until the inert equilibrium trajectory is reached whereat stable extension along this trajectory occurs until instability and failure at ($C_{\max}$, $S_{\max}$). The full trajectories for ideal reactive, realistic reactive and inert failure are shown in Fig. 14 (using for clarity an exaggerated value of $\mathbf{T}_0 = 1.5$), highlighting the truncated precursor extension under reduced χ conditions.

Fig. 15 shows representative experimental observations of applied stress-crack length $\sigma_a(c)$ trajectories measured under reactive (air) equilibrium conditions for (001)[110], (001)[100] and polycrystalline indentation samples over the indentation load range 2 N to 50 N. In nearly every (001)[110] and polycrystalline case, stable precursor extension of a crack from c_1 was observed prior to failure at (c_{min}, σ_{min}), consistent with the representation in Fig. 14 of the effects of a reduced χ value: initial loading to a substantial fraction of the failure stress with very little crack extension, followed by extension with relative magnitudes significantly reduced from the ideal value of 2.52, varying from 2 down to 1 at larger loads, with an average $c_{min}/c_1=1.5$. (This behavior is comparable to that observed previously on {111} specimens [26].) The observations were marked by erratic—almost stick-slip like—crack advance, in which the surface traces of the cracks would remain stationary during many stress increments followed by a large amount of crack extension on one stress increment. This behavior would often not be well correlated between cracks either side of the indentation, suggesting a local rather than a global cause. Previous work on polycrystalline oxides has suggested that such observations are related to the variable formation and rupture of grain-localized interfacial frictional tractions behind the crack tip [130, 131]. Such tractions form when either (a) predominantly intergranular or (b) cleavage dominated transgranular fracture enforce localized sections of the crack path to jog under mixed-mode loading and thence separate with considerable frictional resistance to shear. Some combination of (a) and (b) might account for the observations of the crack extension in the polycrystalline Si. Only (b) is possible for the single crystal materials, with the jogs being (perhaps) formed by local tilts (mode-II) or twists (mode-III) of the crack front on to the alternative secondary ($\bar{1}$ 10) cleavage plane (parallel to the applied stress, perpendicular to the principal crack plane) or one of the primary {111} cleavage planes (inclined to both the applied stress and the principal crack plane).

The $\sigma_a(c)$ trajectories for the (001)[100] indentation specimens were consistent with the observations of greatly enhanced lateral cracking in this orientation (leading to extreme decreases in χ) and the enforced propagation of cracks on the (100) cleavage plane (increased T). Very little precursor crack extension was observed before failure in all cases, varying from 1.7 to 1 at all loads, with an average $c_{min}/c_1=1.2$. Many of the cracks in this orientation probably began with the condition $c_1 > c_{min}$, such the cracks remained metastably trapped throughout the loading process before spontaneous failure at a stress level $< \sigma_{min}$ to the right of the maximum in Fig. 14. The inert strength data of Fig. 12 suggest that enhanced lateral cracking in the (001)[110] orientation at very large indentation loads lead to the condition $c_1 > c_{max}$, such the cracks remained similarly metastably trapped throughout

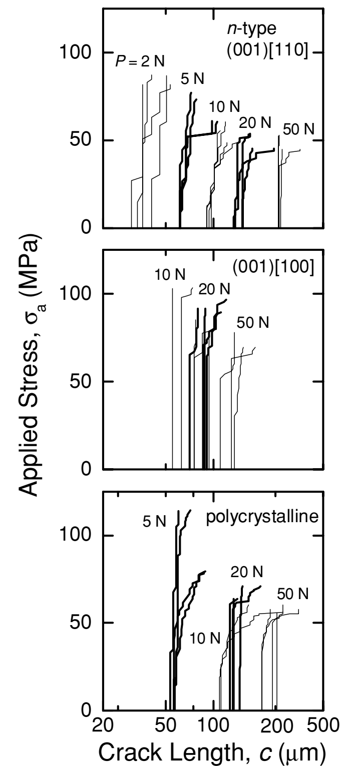

Figure 15 Representative equilibrium applied stress-indentation crack length, σ_a-c, trajectories for Si in air: *n*-type (001)[110], *n*-type (001)[100] and polycrystalline. Each line represents the response of a single crack under uniaxial stress at the indentation load indicated.

the inert stressing process before spontaneous failure at a stress level $< \sigma_{max}$, and thus below the best-fit solution.

Fig. 16 compares the [110] biaxial inert strength results of Fig. 12 (solid lines) with the [110] and [100] uniaxial reactive strength results from all the materials along with some [100] biaxial inert strength results (symbols); all surfaces are (001), see Figs 6a and b. In all cases, for a given geometry and test environment, the [100] indentation strengths were greater than the [110] strengths, although the difference was far less pronounced under biaxial conditions than under uniaxial conditions, suggesting there was a degree of frustration for crack propagation under uniaxial loading. Under biaxial loading, the most potent element of the indentation flaw is free to couple to the stress field in any orientation; this is not so under uniaxial loading, leading to an enforced decrease in ψ for uniaxially-stressed [100] indentations compared with those stressed biaxially. This effect should be minimal for [110] indentations aligned along cleavage planes as there is always a well-defined crack able to couple to the stress field. However, in all cases, the [110] uniaxial strengths measured in air were depressed about 20% relative to the [110] biaxial inert strengths, raising the possibility that there is an effect of atmospheric moisture on the fracture surface energy and observable fracture properties of Si. The case for a reactive environmental effect

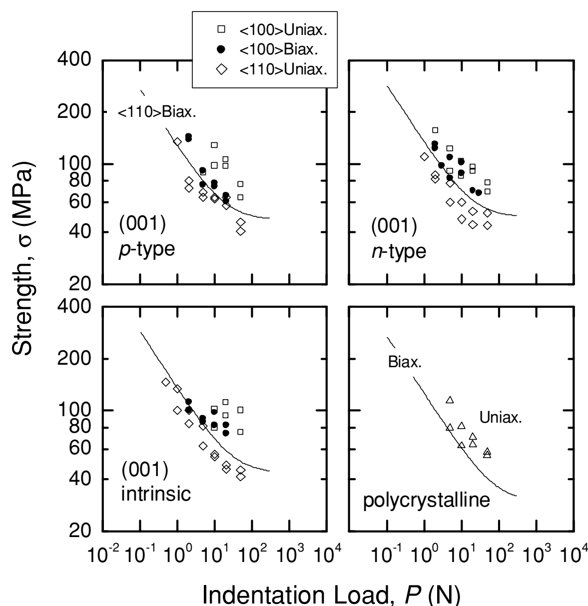

Figure 16 Composite plots of the indentation-strength responses of Si, allowing comparison of indentation orientation, (001)[110] vs (001)[100], and stressing geometry, uniaxial vs biaxial flexure. The solid lines are the <110> biaxial inert best fits from Fig. 12, plotted over the range of experimental observations. The symbols represent individual measurements. The uniaxial measurements were performed in ambient air.

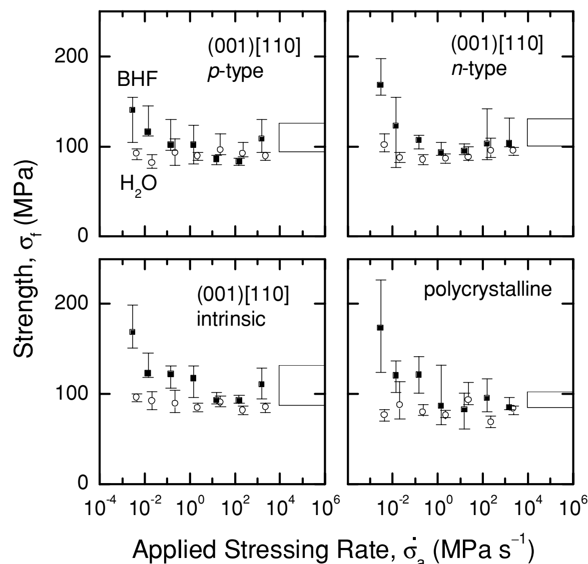

Figure 17 Plots of reactive strength, σ_f, as a function of (constant) applied stressing rate $\dot{\sigma}_a$ for Si containing 2 N Vickers indentation flaws in water (open symbols) and buffered HF solution (BHF, solid symbols). The symbols represent means and limits for at least three-four strength tests at each rate. The open boxes on the left of the plots represent the appropriate inert strength limits.

would be strengthened if the [100] and polycrystalline uniaxial and biaxial strengths had not exhibited the opposite trend, although these data were certainly affected by the frustration effects of uniaxial loading. However, no "slow" crack growth was observed in the crack propagation measurements—including the well-known extended holds at 99% of the failure stress—suggesting that if there was an environmental effect it was extremely rapid.

4.5. Reactive strength

Fig. 17 shows the strength, σ_f, of Si measured under reactive conditions of (liquid) water and aqueous buffered HF (BHF) solution as a function of applied stressing rate, $\dot{\sigma}_a$. The strengths measured in water exhibited no significant variation over a factor of 10^6 in stressing rate. This invariance has been observed previously [90, 91], but is here extended a factor of 100 in stressing rate to failure times of ∼50 ms. Such invariance is typically regarded as a lack of susceptibility of a brittle material to environmentally-enhanced non-equilibrium crack extension. Conversely, a decrease in strength with decreasing stressing rate indicates a susceptibility to non-equilibrium crack growth with kinetics comparable to those of the experiment [134]. This decrease, however, is bounded thermodynamically by the inert strength limit at large stressing rates (the "Griffith" strength) and by the reactive strength limit at small stressing rates (the "Orowan" strength) [134].The important point here is that in all cases the invariant water response was lower in strength than the inert response, indicated on the right of the plots by the open boxes. It is possible then that the invariant water response was at the reactive Orowan limit, suppressed relative to the inert Griffith response by about 20%, and that a kinetically-limited strength variation between the two exists at stressing rates even greater than those used here.

BHF is known to react with Si to form low energy Si–H terminated surfaces, and hence could be expected to exhibit the familiar decrease in reactive strength with decreasing stressing rate. However, as shown in Fig. 17, reactive strengths measured in BHF exhibited increases in strength with decreasing stressing rate, particularly for failure times greater than ∼1000 s, and exhibited greater scatter than those measured in water. The key to this apparently anomalous behavior is that BHF is a corrodant of Si: it reacts with Si surface moieties to actually remove material [100], raising the possibility of indentation- and crack-geometry changes. Fig. 18 shows results testing the idea that it was corrosion rather than stress-corrosion that dominated the strengthening behavior in BHF. The reactive strength data of Fig. 17 are re-plotted in Fig. 18 as a function of time of exposure to the reactive environment (the failure time, $\sigma_f/\dot{\sigma}_a$) as connected symbols; the inert strength bounds are indicated by horizontal lines. Individual symbols represent the inert strengths of samples measured after zero-stress aging at the exposure times indicated. In all cases, exposure to the BHF environment for a given time caused exactly the same strength increase, with or without the application of stress or the presence

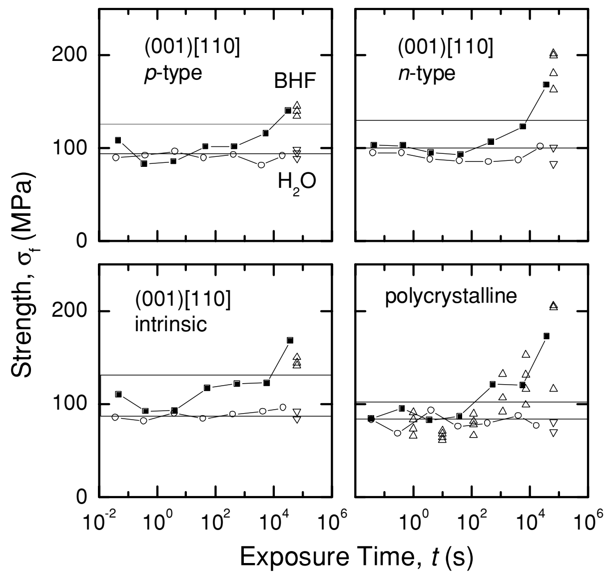

Figure 18 Plots of strength, σ, for Si containing 2 N Vickers indentation flaws as a function of exposure time, t, in water and buffered HF solutions. The open circles and solid squares are the means of constant stressing rate reactive strength tests in water and BHF, respectively, converted from the data of Fig. 17. The upward and downward triangles are individual measurements of inert strength, following zero-stress aging in water and BHF, respectively.

of the environment during failure. Control samples aged in water exhibited inert strengths consistent with those of un-aged samples (if somewhat smaller, suggesting that perhaps not all the water was removed in the air-drying process).

Fig. 19 is a series of micrographs supporting the idea that the strengthening on BHF exposure was caused by corrosion process—but not of the strength-controlling half-penny cracks. Comparison of the (a) as-indented and (b) 2 h exposure surface in Fig. 19 shows that exposure lead to the formation and removal of a lateral crack chip adjacent to the contact impression, the delineation of shear faults and removal of material within the contact zone (bright regions on the scanning electron micrograph indicate loose, "charging" material) and closure of the half-penny surface crack traces. These trends were continued in the 18 h exposure, as shown in Fig. 19c. Similar to a previous study in which lateral crack extension on BHF exposure was monitored by optical microscopy [102], none of the changes above were observed on indentations exposed to water. The observations suggest that BHF exposure lead to strengthening of the indented samples by removing the constraint on the plastic deformation zone by lateral crack formation and, especially, by direct removal of the zone through etching, thus reducing the residual stress-intensity factor amplitude χ. The enlarged view of Fig. 19c in Fig. 20 shows that half-penny cracks are still present but closed and that the remaining material in the contact zone has little integrity.

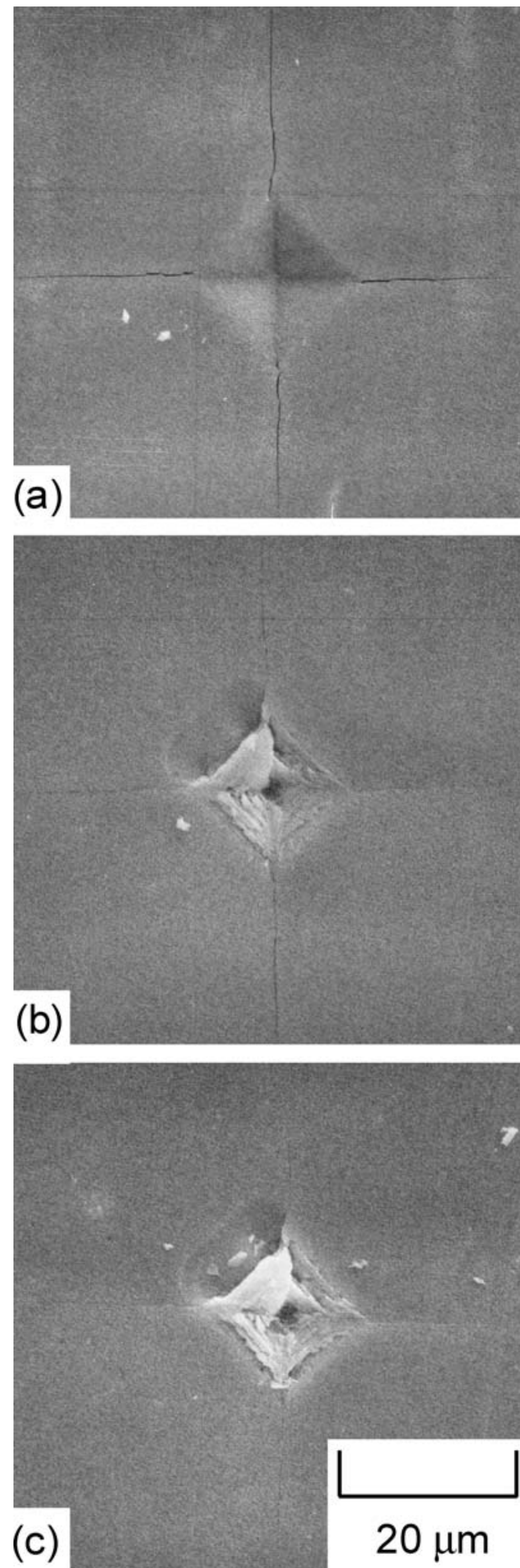

Figure 19 Scanning electron micrographs of a 2 N Vickers (001)[110] indentation in p-type Si showing the appearance of lateral cracks, the etching of the contact impression and the closure of the half-penny cracks during zero-stress aging in buffered HF solution: (a) as-indented; (b) 2 h exposure; and (c) 18 h exposure..

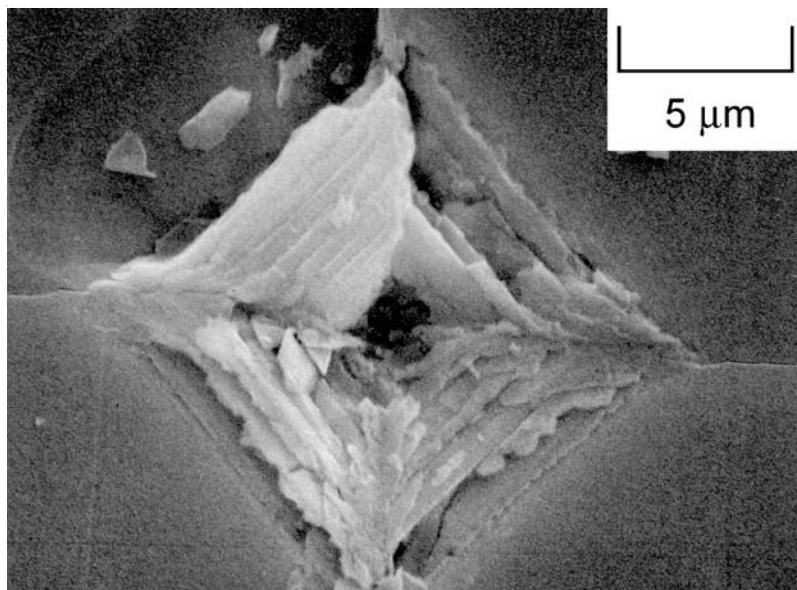

Figure 20 An enlarged view of the contact impression from Fig. 19c, showing etched shear faults and closed half-penny crack traces after 18 h exposure to buffered HF solution.

As discussed above, wafer and die strength can be increased by etching surfaces containing strength-controlling sharp contact flaws remnant from the slicing or back-side grinding process [37, 38, 41]. The BHF aging study above suggests that such strengthening derives from a (somewhat variable) reduction in a component of the crack driving force, rather than a "blunting" of the crack tip and a fundamental change in the nature of the flaw. A previous study on soda-lime glass, in which half-penny and lateral crack lengths and inert strengths all increased to plateau values on water aging came to the same conclusion [135]: strengthening was caused by a reduction in χ (due to lateral crack growth) and not by any change in crack tip geometry. This is not to say that other, stronger, etching media could not have other effects. In fact, observations of indentations in Si aged in Cr_2O_3-based Sirtl etches reveal removal of the plastic deformation zone and adjacent material and significant widening and blunting of the half-penny crack surface traces [136]. Optical interferometric measurements of grinding scratches in Si exposed to plasma etching reveal the formation of U-shaped grooves that were associated with die strengthening [43].

4.6. Fragmentation

Finally, we turn our attention to the fragmentation phenomenon that occurs when the strength of a Si component is exceeded; one of the most easily visible, and sometimes alarming, reminders of the brittleness of Si. It has been known since the earliest studies of fracture, and fracture of Si, that stronger components break into many more pieces—they fragment—compared with weaker components—which may simply break in two. Examples of this are given in Figs 21 and 22 which show increasing levels of fragmentation with increasing inert strength of indented (001)[110] single crystal and polycrystalline Si disk samples. The energy balance of this is simple: the elastic strain energy stored in the sample at failure is converted into surface energy and kinetic energy in the early, adiabatic, stages of dynamic fracture after failure,

$$\frac{\sigma_f^2}{2E} V \rightarrow 2\gamma A + U_K. \tag{24}$$

This conversion is maintained as the failure strength, σ_f, is increased by increases in the cracked surface area/component volume, A/V, i.e., more fragments are formed. (The kinetic energy, U_K, deposited in the velocity of the fragments, tends to increase as well; hence the sometimes alarming nature of the process.)

The mechanism of crack bifurcation required for fragmentation is less easily specified, although it is well known that at large crack velocities ($\sim$0.4 v_R) crack-tip stress fields are distorted so as to have lobes of maximum tension at an angle to the propagation direction [137]. Experimentally, critical crack driving forces are associated with branching (and with mist and hackle formation) [116]. The atomic-scale dynamic fracture simulations show that that the geometry of a rapidly moving crack tip is far from stable [106–108], with branch-like instabilities occurring at extremely large crack velocities and hence driving forces (to leave a rough fracture surface). Such instabilities are likely the initiating points for bifurcation of the crack into two fronts that initially propagate

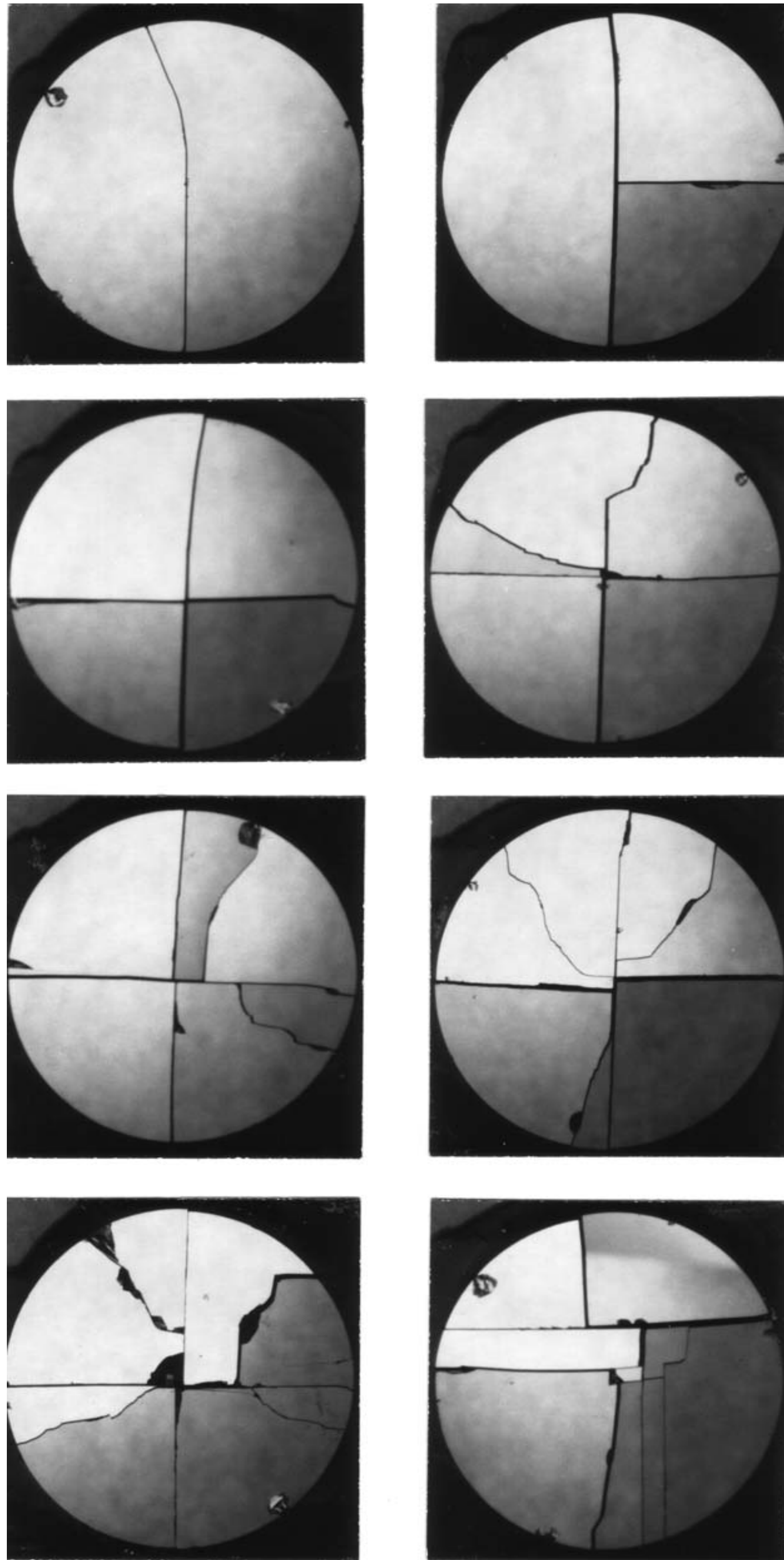

Figure 21 Optical micrographs of the quadrilateral fragmentation patterns formed after failure in biaxial flexure of single crystal *p*-type Si disks containing (001)[110] indentation flaws (disk diameter 35 mm). The number of fragments and failure stress increase from top left to bottom right as shown in Fig. 23, from 2 fragments, 54.3 MPa to 9 fragments, > 215 MPa (stress at center, failure not from indentation but about 30% towards outer edge).

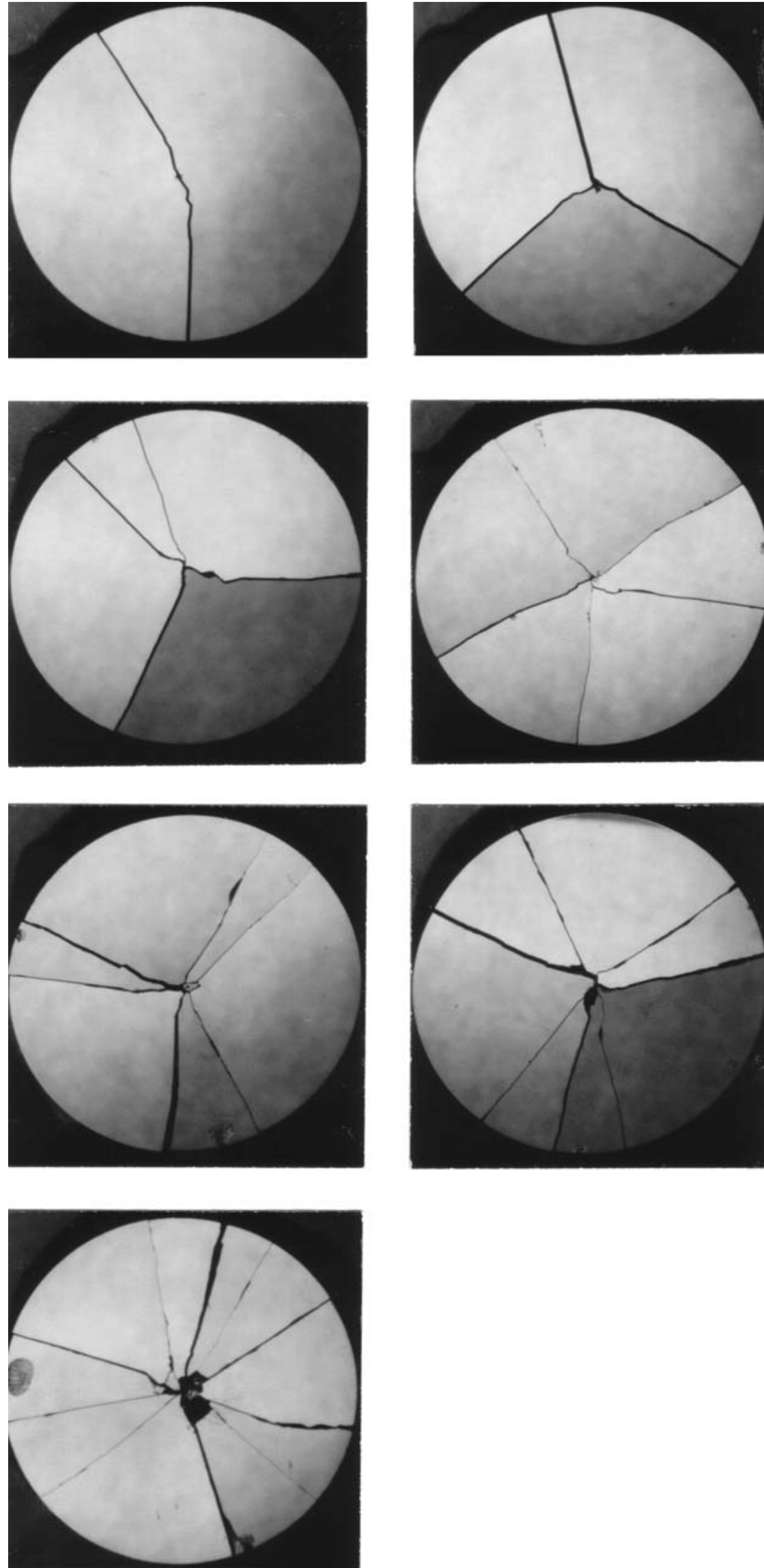

Figure 22 Optical micrographs of the circular sector fragmentation patterns formed after failure in biaxial flexure of polycrystalline Si disks containing indentation flaws (disk diameter 35 mm). The number of fragments and failure stress increase from top left to bottom right as shown in Fig. 23, from 2 fragments, 30.2 MPa to 10 fragments, 286.4 MPa.

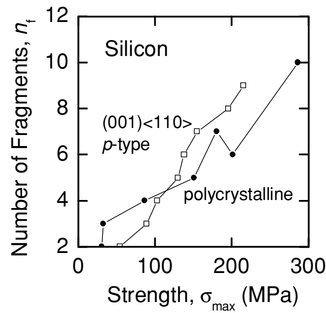

Figure 23 Plot of the number of fragments, n_f, as a function of the failure stress σ_f, for the Si disks shown in Figs 21 and 22.

along the lobes of tension. It is clear from Figs. 21 and 22 that there are strong crystallographic effects in the fragmentation of Si, consistent with the elastic anisotropy (and hence the shape of the tensile lobes at large crack velocities). The biaxially flexed single crystal disks developed rectangular-shaped fragments, whereas the polycrystalline disks developed wedge-shaped fragments (similar to other polycrystalline and amorphous materials). The results suggest that crystallographic cleavage and elastic anisotropy greatly affect the stress- and crack-initiation fields of rapidly propagating (km s^{-1}) cracks.

Fragmentation patterns are of some practical utility with regard to post-failure strength analyses. Reconstruction of samples, such as in Figs 21 and 22, clearly provides a method for identifying the fracture initiating point and strength-limiting defect; although it can be seen that for highly fragmented samples this is difficult. The relation between the number of fragments and the failure stress provides a method for determining whether a component failed because it contained a large flaw or was over-stressed. Fig. 23 is a plot of the number of fragments formed as a function of the failure stress for the disks in Figs 21 and 22. Such correlations may be used as a diagnosis for the stress at failure of a Si device [41], similar to other fractographic techniques [116].

5. Current status and challenges

Controlled flaws in the form of Vickers indentations are extremely good models of the sharp particle damage introduced by slicing, grinding and dicing of wafers and dice during Si manufacturing processes. An indentation formed by a peak contact load of 1 N limits the strength of a Si component to about 120 MPa; the center of the range observed for finished wafers and dice. The characteristic dimension of such an indentation is about 10 μm, consistent with the scale of the damage observed on ground surfaces and diced edges. The power of indentation techniques in process design and control and failure analysis can then be seen in plots such as those of Figs 8 and 12. Controlled variation of the contact load about this mid-point allows indentation dimensions to be systematically decreased or increased, with attendant increases or decreases in strength, such that variations in process conditions can be explored or diagnosed. In fact, Figs 8 and 12 provide exactly the quantitative linkage suggested in the overview as required between a controllable processing variable (the peak contact load of a sharp particle, or its residual deformation) and the dependent component performance (the survivability of a wafer or die, or its strength). The large strength and contact load ranges of Figs 8 and 12 suggest that these should suffice as design diagrams for most wafer, die or packaging processes. Extensions could be made easily, however, for variability due to flaw or loading orientation (Fig. 16), quantification of flaw size by the extremely visible lateral cracks [124, 129] or ultra high-strength wafers by including sub-threshold flaws [74, 75].

The broad agreement between the indentation deformation, fracture and strength parameters measured here with those determined previously, Tables II and III, further confirms the quantitative usefulness of the experiments here for design purposes. Many, if not overwhelmingly most, previous authors have chosen to tabulate compilations of reported toughness values in confirming their work. This is not done here for several reasons: many workers do not report enough analytical detail to allow a firm linkage between the experimental measurable and the reported quantity; given the observations of Figs 9 and 10, it is likely that many "off-axis" indentations resulted in non-ideal patterns with ill-defined half-penny crack traces; fractographic-based methods suffer from ambiguity of flaw-size and residual stress state. Hence, the raw invariant indentation parameters, $P/c^{3/2}$ and $\sigma P^{1/3}$, are compared here, as reported, or determined from presented data. With appropriate qualification, these may be used to estimate the toughness from inversion of Equations 12b and 17

$$T_{\text{air}} = \xi_0 (E/H)^{1/2} P/c_1^{3/2} \tag{25a}$$

$$T_0 = \eta (E/H)^{1/8} \left(\sigma_{\max}^P P^{1/3}\right)^{3/4} \tag{25b}$$

where Equation 10 has been used. The best-calibrated estimates of the pre-factors are [138] $\xi_0 = 0.016$ and [139] $\eta = 0.52$. Representative values of $P/c_1^{3/2}$ and H for the (001)[110] indentations reported here are 11.5 MPa $m^{1/2}$ and 10.3 GPa, which, on using the *polycrystalline* modulus of $E = 163$ GPa, appropriate to an indentation stress field [28] gives $T_{\text{air}} \sim 0.73$ MPa $m^{1/2}$. A representative value of $\sigma_{\max}^P P^{1/3}$ for the (001)[110] indentations here is 130 MPa $N^{1/3}$, which, with the same E and H values, gives $T_0 \sim 0.89$ MPa $m^{1/2}$. These estimates agree with the predictions of Fig. 3c to within the 25% uncertainty

inherent in the calibration factors [138, 139], but little more can be said. Use of the appropriate single crystal moduli in Equation 3 to estimate γ, after T estimates as above, generates values much greater than those in Fig. 3b with no clear minimum for $\gamma_{(111)}$. The underlying fracture surface anisotropy of Si can certainly not be gleaned from Tables II and III or Fig. 16 with one important exception. Indentation orientations that generate lateral cracking are associated with significant suppression and distortion of half-penny cracks and mild increases in strength. These effects derive from changes in indentation geometry not from increases in fracture resistance experienced by half-penny cracks on well-defined fracture planes. The suppression of pre-cursor crack extension on applied stressing, Fig. 15, also points to a decrease in the residual field rather than an increase in fracture resistance for misoriented indentations.

The original fracture resistance measurements [6, 7] using a well-defined, plane-strain double cantilever beam geometry are still the best, but certainly worth repeating in this regard. Modern techniques of displacement and moment control and fast data acquisition, along with ease of obtaining large, appropriately oriented single crystals should allow questions regarding fracture anisotropy and path stability to be answered. Such tests would also allow the still-tantalising effects of environment to be studied. The results here suggest that Si is mildly susceptible to chemical reaction with water under fracture conditions and that the effect is extremely rapid ($<$50 ms) in decreasing the surface energy by about 20–30%. The results also suggest that Si is extremely susceptible to reactive attack by buffered HF, leading to a slow ($>$100 s) increase in strength associated with residual stress relief. Both of these observations would benefit from direct measurements of fracture resistance and kinetics in a reactive environment using a well defined geometry.

Acknowledgements
The author thanks Eric Liniger and Andrea Grant for their meticulous assistance with the experiments and Michelle Oyen for assistance with data analysis and discussions of the manuscript.

References

1. A. KELLY and G. W. GROVES, "Crystallography and Crystal Defects" (Longman Group Limited, London, 1970).
2. G. A. WOLFF and J. D. BRODER, *Acta Cryst.* **12** (1959) 313.
3. J. F. NYE, "Physical Properties of Crystals" (Oxford University Press, Oxford, 1979)
4. Z. HASHIN and S. SHTRIKMAN, *J. Mech. Phys. Solids.* **10** (1962) 343.
5. W. D. HARKINS, *J. Chem. Phys.* **10** (1942) 268.
6. J. J. GILMAN, *J. Appl. Phys.* **31** (1960) 3208.
7. R. J. JACODINE, *J. Electrochem. Soc.* **110** (1963) 524.
8. G. R. IRWIN, in "Handbuch der Physik," edited by S. Flügge (Springer-Verlag, Berlin-Heidelberg, 1958) p. 551.
9. G. C. SIH, P. C. PARIS and G. R. IRWIN, *Int. J. Fracture Mech.* **1** (1965) 189.
10. K. L. JOHNSON, "Contact Mechanics" (Cambridge University Press, Cambridge, 1985).
11. S. G. ROBERTS, P. PIROUZ and P. B. HIRSCH, *J. de Physique* **44** (1983) C4–75
12. G. C. RYBICKI and P. PIROUZ, "Indentation Plasticity and Fracture in Silicon," NASA Technical Paper 2863 (NASA Lewis, Cleveland, 1988)
13. G. M. PHARR, W. C. OLIVER and D. R. CLARKE, *J. Electronic. Mater.* **19** (1990) 881.
14. D. R. CLARKE, M. C. KROLL, P. D. KIRCHNER, R. F. COOK and B. J. HOCKEY, *Phys. Rev. Letters* **60** (1988) 2156.
15. S. JOHANSSON and J.-A. SCHWEITZ, *J. Am. Ceram. Soc.* **71** (1988) 617.
16. J. C. MORRIS and D. L. CALLAHAN, *J. Mater. Res.* **9** (1994) 2907.
17. H. SAKA and S. ABE, *J. Electron Microscopy* **1** (1997) 45.
18. A. B. MANN, D. VAN HEERDEN, J. B. PETHICA and T. P. WEIHS, *J. Mater. Res.* **15** (2000) 1754.
19. J. T. HAGAN, *J. Mater. Sci.* **14** (1979) 2975.
20. *Idem.*, *ibid.* **15** (1980) 1417.
21. K. E. PUTTICK and M. M. HOSSEINI, *J. Phys. D: Appl. Phys.* **13** (1980) 875.
22. L. CHAO, K. J. MA, D. S. LIU, C. Y. BAI and T. L. SHY, *J. Mater. Processing Technol.* **127** (2002) 187.
23. J. YAN, K. SYOJI and J. TAMAKI, *Wear* **255** (2003) 1380.
24. W. C. OLIVER and G. M. PHARR, *J. Mater. Res.* **7** (1992) 1564.
25. B. R. LAWN, A. G. EVANS and D. B. MARSHALL, *J. Am. Ceram. Soc.* **63** (1980) 574.
26. B. R. LAWN, D. B. MARSHALL and P. CHANTIKUL, *J. Mater. Sci.* **16** (1981) 1769.
27. B. R. LAWN, *J. Appl. Phys.* **39** (1968) 4828.
28. J. J. VLASSAK and W. D. NIX, *J. Mech. Phys. Solids* **42** (1994) 1223.
29. A. A. GRIFFITH, *Phil. Trans. Roy. Soc.* **A221** (1921) 163.
30. L. D. DYER, *J. Cryst. Growth* **85** (1987) 75.
31. M. S. BAWA, E. F. PETRO and H. M. GRIMES, *Semicond. Intern.* **18** (1995) 115.
32. R. F. COOK and G. M. PHARR, *J. Am. Ceram. Soc.* **73** (1990) 787.
33. G. L. PEARSON, W. T. READ JR, and W. L. FELDMANN, *Acta Met.* **5** (1957) 181.
34. S. M. HU, *J. Appl. Phys.* **53** (1982) 3576.
35. J. C. MCCLAUGHLIN and A. F. W. WILLOUGHBY, *J. Cryst. Growth* **85** (1987) 83.
36. J. VEDDE and P. GRAVESEN, *Mat. Sci. Eng.* **B36** (1996) 246.
37. C. FUNKE, E. KULLIG, M. KUNA and H. J. MÖLLER, *Advanced Eng. Mater.* **6** (2004) 594.
38. S.-M. JEONG, S.-E. PARK, H.-S. OH and H. L. LEE, *J. Ceram. Proc. Res.* **5** (2004) 171.
39. www.ca.sandia.gov/industry_partner/macwafer1.html, (5/10/2005)
40. K. MCGUIRE, S. DANYLUK, T. L. BAKER, J. W. RUPNOW and D. MCLAUGHLIN, *J. Mater. Sci.* **32** (1997) 1017.
41. B. HUDSON and D. PERRIN, in "Proceedings of International Symposium for Testing and Failure Analysis" (ASM International, Pittsburgh, 1990) p. 515.
42. M. K. GRIEF and J. A. STEELE JR, in "Proceedings International Electronics Manufacturing Symposium" (IEEE, 1996) p.190.
43. N. MCLELLAN, N. FAN, S. LIU, K. LAU and J. WU, *J. Electronic Packaging* **126** (2004) 110.
44. M. HENDRIX and S. DREWS, www.hologenix. com/Article1.htm (5/10/2005).
45. R. MENDELSON, D. DIEFENDERFER, C. GUMBERT and B. SINGH, *Semiconductor International* **19** (1996) 221.

46. B. COTTEREL, Z. CHEN, J.-B. HAN and N. X. TAN, *J. Electronic Packaging* **125** (2003) 114.
47. R. L. MENDELSON, R. F. COOK, D. F. DIEFENDERGER, E. G. LINIGER, J. M. BLONDIN and D. W. BROUILLETTE, United States Patent, 5,888,838 (1999).
48. C. C. CHAO, R. CHLEBOSKI, E. J. HENDERSON, C. K. HOLMES and J. P. KALEJS, in Materials Research Symposium Proceedings. edited by E. Suhir, R. C. Cammarata, and D. D. L. Chung (MRS, Pittsburgh, 1991) Vol. 226, p. 363.
49. S. F. POPELAR, in "Proceedings of Fourth International Symposium on Advanced Packaging Materials," (IMAPS, Washington, 1998) p. 41.
50. S. MICHAELIDES and S. K. SITARAMAN, *IEEE Trans. Advanced Packaging* **22** (1999) 602.
51. S. JOHANSSON and J.-Å. SCHWEITZ, *J. Appl. Phys.* **63** (1988) 4799.
52. C. J. WILSON, A. ORMEGGI and M. NARBUTOVSKIH, *ibid.* **79** (1996) 2386.
53. C. J. WILSON and P. A. BECK, *J. Microelectromech. Sys.* **5** (1996) 142.
54. T. NAMAZU, Y. ISONO and T. TANAKA, *ibid.* **9** (2000) 450.
55. S. SUNDARARAJAN, B. BHUSHAN, T. NAMAZU and Y. ISONO, *Ultramicroscopy* **91** (2002) 111.
56. M. T. A. SAIF and N. C. MACDONALD, in Proceedings of the Ninth Annual International Workshop on Micro Electro Mechanical Systems, (IEEE, New York, 1996) p. 105.
57. K.-S. CHEN, A. AYON and S. M. SPEARING, *J. Am. Ceram. Soc.* **83** (2000) 1476.
58. F. POURAHMADI, D. GEE and K. PETERSON, in Proceedings of International Conference on Sensors and Actuators, (IEEE, New York, 1991) p. 197.
59. E. MAZZA and J. DUAL, *J. Mech. Phys. Solids* **47** (1999) 1795.
60. W. SUWITO, M. L. DUNN, S. J. CUNNINGHAM and D. T. READ, *J. Appl. Phys.* **85** (1999) 3519.
61. S. GREEK, F. ERICSON, S. JOHANSSON and J.-Å. SCHWEITZ, in " Digest of Technical Papers, Eighth International Conference on Solid State Sensors and Actuators" (Foundation for Sensors and Actuators Technology, 1995) p. 56.
62. H. BIEBL and H. VON PHILIPSBORN, in " Digest of Technical Papers, Eighth International Conference on Solid State Sensors and Actuators" (Foundation for Sensors and Actuators Technology, 1995) p. 72.
63. W. SUWITO, M. L. DUNN and S. J. CUNNINGHAM, *J. Appl. Phys.* **83** (1998) 3574.
64. O. M. JADAAN, N. N. NEMETH, J. BAGDAHN and W. W. SHARPE JR, *J. Mater. Sci.* **38** (2003) 4087.
65. M. F. ASHBY "Materials Selection in Mechanical Design, Second Edition" (Butterworth Heinemann, Oxford, 1999).
66. C. P. CHEN and M. H. LEIPOLD, *Ceram. Bulle.* **59** (1980) 469.
67. C. P. CHEN, M. H. LEIPOLD JR and D. HELMREICH, *J. Am. Ceram. Soc.* **65** (1982) C-49.
68. K. YASUTAKE, M. IWATA, K. YOSHII, M. UMENO and K. KAWABE, *J. Mater. Sci.* **21** (1986) 2185.
69. Y. L. TSAI and J. J. MECHOLSKY JR, *J. Mater. Res.* **6** (1991) 1248.
70. K. HAYASHI, S. TSUJIMOTO, Y. OKAMOTO and T. NISHIKAWA, *J. Soc. Mater. Sci. Japan* **40** (1991) 39.
71. *Idem.*, *ibid.* **41** (1991) 488.
72. D. B. MARSHALL and B. R. LAWN, *J. Mater. Sci.* **14** (1979) 2001.
73. D. B. MARSHALL, B. R. LAWN and P. CHANTIKUL, *ibid.* 2225.
74. A. PAJARES, M. CHUMAKOV and B. R. LAWN, *J. Mater. Res.* **19** (2004) 657.
75. Y.-G. JUNG, A. PAJARES, R. BANERJEE and B. R. LAWN, *Acta Mat.* **52** (2004) 3459.
76. D. J. MORRIS, S. B. MYERS and R. F. COOK, *J. Mater. Res.* **19** (2004) 165.
77. D. R. CLARKE, in "Semiconductors and Semimetals," edited by K. T. Faber and K. Malloy (Academic Press, 1992) p. 79.
78. C. P. CHEN and M. H. LEIPOLD, in "Fracture Mechanics of Ceramics," edited by R. C. Bradt, A. G. Evans, D. P. H. Hasselman and F. F. Lange (Plenum Press, New York, 1986) p. 285.
79. S. B. BHADURI and F. F. Y. WANG, *J. Mater. Sci.* **21** (1986) 2489.
80. C. MESSMER and J. C. BILELLO, *J. Appl. Phys.* **52** (1981) 4623.
81. Y.-B. XIN and K. J. HSIA, *Acta Mater.* **44** (1996) 845.
82. A. M. FITZGERALD, R. H. DAUSKARDT and T. W. KENNY, *Sensors and Actuators* **83** (2000) 194.
83. X. LI, T. KASAI, S. NAKAO, T. ANDO, M. SHIKIDA, K. SATO and H. TANAKA, *ibid.* **117** (2005) 143.
84. X. LI, T. KASAI, S. NAKAO, H. TANAKA, T. ANDO, M. SHIKIDA and K. SATO, *ibid.* 229.
85. R. BALLARINI, R. L. MULLEN, Y. YIN, H. KAHN, S. STEMMER and A. H. HEUER, *J. Mater. Res.* **12** (1997) 915.
86. R. C. BRODIE and D. F. BAHR, *Mater. Sci. Engin.* **A351** (2003) 166.
87. H. KAHN, R. BALLARINI, J. J. BELLANTE and A. H. HEUER, *Science* **298** (2002) 1215.
88. B. WONG and R. H. HOLBROOK, *J. Electrochem. Soc.* **134** (1987) 2254.
89. T.-J. CHEN and W. J. KNAPP, *J. Am. Ceram. Soc.* **63** (1980) 225.
90. C. P. CHEN and M. H. LEIPOLD, *ibid.* **68** (1985) C-54.
91. C.-S. LEE, D. Y. KIM, J. SÁNCHEZ, P. MIRANDA, A. PAJARES and B. R. LAWN, *ibid.* **85** (2002) 2019.
92. A. M. FITZGERALD, R. SURYANARARAYANAN, R. H. DAUSKARDT and T. W. KENNY, in "Proceedings of Micro-Electron-Mechanical Systems, DSC—Vol. 66" (ASME, Pittsburgh, 1998) p. 395.
93. S. B. BHADURI and F. F. Y. WANG, in "Fracture Mechanics of Ceramics," edited by R. C. Bradt, A. G. Evans, D. P. H. Hasselman and F. F. Lange (Plenum Press, New York, 1983) p. 327.
94. J. A. CONNALLY and S. B. BROWN, *Science* **256** (2002) 1537.
95. L. MUHLSTEIN and R. O. RITCHIE, *Int. J. Fracture* **119/120** (2003) 449.
96. T. A. MICHALSKE and S. W. FREIMAN, *Nature* **295** (1982) 511.
97. W. WONG-NG, G. S. WHITE, S. W. FREIMAN and C. G. LINDSAY, *Computational Mater. Sci.* **6** (1996) 63.
98. S. OGATA, F. SHIMOJO, R. K. KALIA, A. NAKANO and P. VASHISHSTA, *J. Appl. Phys.* **96** (2004) 5316.
99. G. S. HIGASHI, Y. J. CHABAL, G. W. TRUCKS and K. RAGHAVACHARI, *Appl. Phys. Lett.* **56** (1990) 656.
100. G. W. TRUCKS, K. RAGHAVACHARI, G. S. HIGASHI and Y. J. CHABAL, *Phys. Rev. Lett.* **65** (1990) 504.
101. G. S. HIGASHI, in "The Physics and Chemistry of SiO_2 and and the Si-SiO_2 Interface," edited by C. R. Helms and B. E. Deal. (Plenum Press, New York, 1993) p. 187.
102. M. D. THOULESS and R. F. COOK, *Appl. Phys. Lett.* **56** (1990) 1962.
103. E. SINCLAIR and B. R. LAWN, *Proc. R. Soc. Lond. A.* **239** (1972) 83.
104. J. HAUCH, D. HOLLAND, M. P. MARDER and H. L. SWINNEY, *Phys. Rev. Letters* **82** (1999) 3823.
105. D. SHERMAN and I. BE'ERY, *ibid.* **93** (2004) 265501-1
106. D. HOLLAND, M. P. MARDER, *ibid.* **80** (1998) 746.
107. F. ABRAHAM, N. BERNSTEIN, J. Q. BROUGHTON and D. HESS, *MRS Bulletin* **25** (2000) 27.

108. J. SWADENER, M. I. BASKES and M. NASTASI, *Phys. Rev. Lett.* **89** (2002) 085503-1.
109. A. M. LOMONOSOV and P. HESS, *ibid.* **89** (2002) 095501-1.
110. G. LEHMANN, A. M. LOMONOSOV, P. HESS and P. GUMBSCH, *J. Appl. Phys.* **94** (2003) 2907.
111. R. PÉREZ and P. GUMBSCH, *Phys. Rev. Lett.* **84** (2000) 5347.
112. N. P. BAILEY and J. P. SETHNA, *Phys. Rev. B* **68** (2003) 205204-1.
113. M. V. SWAIN, B. R. LAWN and S. J. BURNS, *J. Mater. Sci.* **9** (1974) 175.
114. J. KAUFMAN and A. J. FORTY, *ibid.* **21** (1986) 3167.
115. Y.-B. XIN, K. J. HSIA and D. A. LANGE, *J. Am. Ceram. Soc.* **78** (1995) 3201.
116. Y. L. TSAI and J. J. MECHOLSKY JR, *Int. J. Fracture* **57** (1992) 167.
117. D. SHERMAN, *J. Mater. Sci.* **38** (2003) 783.
118. L. D. DYER, in "Semiconductor Processing," edited by D. C. Gupta (ASTM, Philadelphia, 1984) p. 297.
119. R. MARKS, *Int. J. Microcirc. Electro. Pack.* **16** (1993) 350.
120. J. THURN, D. J. MORRIS and R. F. COOK, *J. Mater. Res.* **17** (2002) 2679.
121. J. THURN and R. F. COOK, *ibid.* **19** (2004) 124.
122. R. J. ROARK and W. C. YOUNG, "Formulas for Stress and Strain, Fifth Edition" (McGraw-Hill, Japan, 1976).
123. R. TANDON and R. F. COOK, *J. Am Ceram. Soc.* **76** (1993) 885.
124. D. B. MARSHALL, B. R. LAWN and A. G. EVANS, *ibid.* **65** (1982) 561.
125. R. W. FANCHER, C. M. WATKINS, M. G. NORTON, D. F. BAHR and E. W. OSBORNE, *J. Mater. Sci.* **36** (2001) 5441.
126. F. EBRAHIMI and L. KALWANI, *Mater. Sci. Enging.* **A268** (1999) 116.
127. J. G. SWADENER and M. NASTASI, *J. Mater. Sci. Lett.* **21** (2002) 1363.
128. R. F. COOK and D. H. ROACH, *J. Mat. Res.* **1** (1986) 589.
129. R. F. COOK, M. R. PASCUCCI and W. H. RHODES, *J. Amer. Cer. Soc.* **73** (1990) 1873.
130. R. F. COOK and E. G. LINIGER, *J. Mater. Sci.* **27** (1992) 4751.
131. R. F. COOK, E. G. LINIGER and M. R. PASCUCCI, *J. Hard Mater.* **5** (1994) 190.
132. K. MASUDO-JINDO and K. MAEDA, *Mater. Sci. Enging.* **A176** (1994) 225.
133. R. F. COOK, *ibid.* **A260** (1999) 29.
134. E. OROWAN, *Nature* **154** (1944) 341.
135. B. R. LAWN, K. JAKUS and A. C. GONZALEZ, *J. Am. Ceram. Soc.* **68** (1985) 25.
136. S. DANYLUK and S.-W. LEE, *J. Appl. Phys.* **64** (1988) 4075.
137. E. YOFFE, *Phil. Mag.* **42** (1951) 739.
138. G. R. ANSTIS, P. CHANTIKUL, B. R. LAWN and D. B. MARSHALL, *J. Am. Ceram. Soc.* **64** (1981) 532.
139. R. F. COOK, C. J. FAIRBANKS, B. R. LAWN and Y.-W. MAI, *J. Mater. Res.* **2** (1987) 345.